PAPER

Comparative oxidative ability of mononuclear and dinuclear high-valent iron–oxo species towards the activation of methane: does the axial/bridge atom modulate the reactivity?†

Mursaleem Ansari* and Gopalan Rajaraman [ID] *

Over the years, mononuclear $Fe^{IV}=O$ species have been extensively studied, but the presence of dinuclear $Fe^{IV}=O$ species in soluble methane monooxygenase (sMMO) has inspired the development of biomimic models that could activate inert substrates such as methane. There are some successful attempts; particularly the $[(Por)(m\text{-}CBA) Fe^{IV}(\mu\text{-}N)Fe^{IV}(O)(Por^{\bullet+})]^-$ species has been reported to activate methane and yield decent catalytic turnover numbers and therefore regarded as the closest to the sMMO enzyme functional model, as no mononuclear $Fe^{IV}=O$ analogues could achieve this feat. In this work, we have studied a series of mono and dinuclear models using DFT and *ab initio* DLPNO−CCSD(T) calculations to probe the importance of nuclearity in enhancing the reactivity. We have probed the catalytic activities of four complexes: $[(HO)Fe^{IV}(O)(Por)]^-$ (**1**), $[(HO)Fe^{IV}(O)(Por^{\bullet+})]$ (**2**), μ-oxo dinuclear iron species $[(Por)(m\text{-}CBA)Fe^{IV}(\mu\text{-}O)Fe^{IV}(O) (Por^{\bullet+})]^-$ (**3**) and *N*-bridged dinuclear iron species $[(Por)(m\text{-}CBA)Fe^{IV}(\mu\text{-}N)Fe^{IV}(O) (Por^{\bullet+})]^-$ (**4**) towards the activation of methane. Additionally, calculations were performed on the mononuclear models $[(X)Fe^{IV}(O)(Por^{\bullet+})]^n$ {X = N **4a** ($n = -2$), NH **4b** ($n = -1$) and NH_2 **4c** ($n = 0$)} to understand the role of nuclearity in the reactivity. DFT calculations performed on species **1–4** suggest an interesting variation among them, with species **1–3** possessing an intermediate spin ($S = 1$) as a ground state and species **4** possessing a high-spin ($S = 2$) as a ground state. Furthermore, the two Fe^{IV} centres in species **3** and **4** are antiferromagnetically coupled, yielding a singlet state with a distinct difference in their electronic structure. On the other hand, species **2** exhibits a ferromagnetic coupling between the Fe^{IV} and the $Por^{\bullet+}$ moiety. Our calculations suggest that the higher barriers for the C−H bond activation of methane and the rebound step for species **1** and **3** are very high in energy, rendering them unreactive towards methane, while species **2** and **4** have lower barriers, suggesting their reactivity towards methane. Studies on the system reveal that model **4a** has multiple $Fe=N$ bonds facilitating greater reactivity, whereas the other two models have longer Fe−N bonds and less radical character with steeper barriers. Strong electronic cooperativity is found to be facilitated by the bridging nitride atom, and this cooperativity is suppressed by substituents such as oxygen, rendering them inactive. Thus, our study unravels that apart from enhancing the nuclearity, bridging atoms that facilitate strong cooperation between the metals are required to activate very inert substrates such as methane, and our results are broadly in agreement with earlier experimental findings.

Introduction

The conversion of hydrocarbons such as methane at low temperatures has long been a challenge for chemists.[1,2] The selective oxidation of the C–H bonds of hydrocarbons is a subject of intensive research in the pursuit of alternative fuels, namely methane to methanol conversion.[1–3] While such reactions are

challenging for chemists, enzymes such as methane monooxygenase (sMMO), cytochrome P450, and cytochrome c peroxidases perform this transformation easily with high selectivity and efficiency.[4–7] The discovery of the powerful oxidation properties of cytochrome P450 associated with its iron-porphyrin active site and understanding the mechanism of natural monooxygenase catalysts[3] have motivated scientists to devote their attention to developing a synthetic model of iron(iv)–oxo species.[4–6,8–10] Biochemically and synthetically, these iron–oxo species are potent activators of inactive C–H bonds.[5,11–17] As a consequence of its biological significance, cytochrome P450 (Cpd I) has been extensively investigated with *in situ* generated

Department of Chemistry, Indian Institute of Technology Bombay, Mumbai 400076, India. E-mail: rajaraman@chem.iitb.ac.in, mansaribhu@gmail.com

oxoiron(IV) porphyrin cation radical complexes in a variety of oxidation reactions, including epoxidation of olefins and hydroxylation of hydrocarbons.[18,19] Cpd I reaction mechanisms have been studied experimentally[5,20,21] and theoretically[21,22] using axial ligands. Compared to Cpd I mimics, Fe(IV)–oxo porphyrins and Cpd II mimics are considered as poor oxidants.[22–27] Recently, Karlin and coworkers reported the effects of various axial ligands as well as presence of Lewis acid on the reactivity of a model system of Cpd II that activate 9,10-dihydroanthracene exemplifying the role of both on the reactivity.[28,29]

The reactivity of this species is correlated with various factors such as the axial ligand, equatorial donation, the nature of ligand donor atoms, and the nature of the ground spin state and leads to the formation of several $Fe^{IV}=O$ species with various ligand architectures such as bispidines,[30–32] salen, corrole, and porphyrin to name a few.[33–38] In addition to the factor mentioned, there is metal nuclearity that also influences the reactivity. Several studies have shown that larger nuclearity species are better catalysts as a result of enhancing the nuclearity of the $Fe^{IV}=O$ complexes from two to five. For example, the pentanuclear $Fe^{IV}=O$ catalyst has been reported[39,40] to split water up to 1000 times faster than a mononuclear iron-based catalyst,[41] and a tetrameric terminal iron–oxo species has been reported to functionalize C–F and C–H bonds of arene hydroxylation electrophilically.[42] It is challenging to understand how nuclearity correlates with reactivity in a larger system of nuclearity, so dinuclear species are the best suited for such studies.[43–47]

Functional models for a μ-oxo-bridged diiron(III) complex have recently received much attention.[48] These complexes act as active sites in several proteins involved in oxygen storage, such as hemerytherin,[49] and oxygen activation, such as methane monooxygenase.[50] In recent years, several synthetic

Fe–O–Fe (μ-oxo) diiron(III) complexes have been synthesised that have shown promising catalase-like activity[51] and can act as catalysts for alkane oxidation.[28,52,53] Recently, Sorokin et al. revealed the superiority of nitrogen bridged complexes over their oxo counterparts in oxidation reactions supported by spectroscopic techniques as well as theoretical calculations on the Fe–X–Fe (X = C, N, O) core.[7,18,54,55] Notably, the complex [(TPP)(m-CBA)Fe^{IV}(μ-N)Fe^{IV}(O)(TPP⁺•)]⁻ has been synthesised and characterised using EPR, UV/Vis, and Mössbauer techniques by Sorokin et al.[56] This complex has shown catalytic activity towards an array of alkanes, including the most difficult ones, such as methane.[56] Apart from the experimental studies, quantum chemical calculations have also helped us to understand the electronic structure of the catalytically active species and explore the mechanism of the catalytic reactions.[57–60]

Over the past few decades, our group has reported several catalytic organic transformations using high-valent metal–oxo species using a combination of DFT and ab initio calculations; particularly we probed the role of electronic cooperativity in dinuclear $Fe^{IV}=O$ in facilitating a greater reactivity. As the electronic cooperativity between two metal centres is found to be fundamental not only in this model system but also in the reactivity of enzymes such as sMMO and related biomimic models,[44,45,61,62] it is imperative to test this hypothesis on mononuclear $Fe^{IV}=O$ with a dinuclear $Fe^{IV}=O$ species. With this objective in mind, in this work, we have performed detailed density functional theory calculations on four complexes [(HO)Fe^{IV}(O)(Por)]⁻ (1), [(HO)Fe^{IV}(O)(Por⁺•)] (2), [(Por)(m-CBA)Fe^{IV}(μ-O)Fe^{IV}(O)(Por⁺•)] (3) and [(Por)(m-CBA)Fe^{IV}(μ-N)Fe^{IV}(O) (Por⁺•)]⁻ (4), (see Scheme 1) to explore the electronic structure and its comparative oxidative ability towards oxidation of extremely difficult substrates such as methane. To analyse and understand the role of nuclearity in facilitating
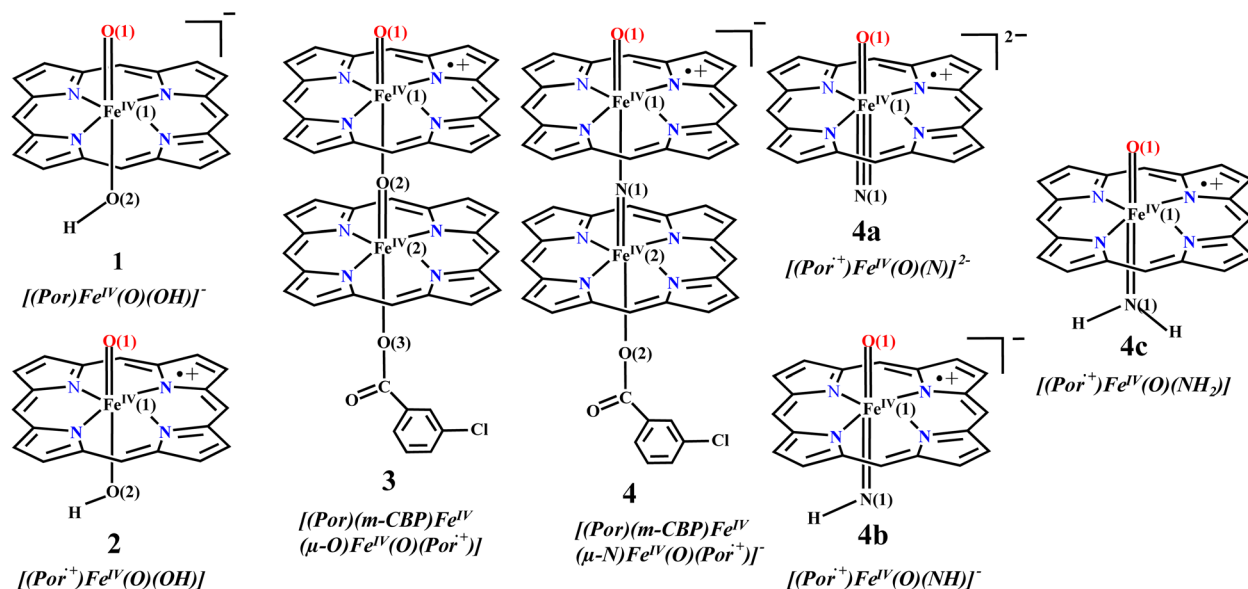
Scheme 1 There are different oxidants used for the C–H bond activation of methane. Species **1** is the model system of Cpd II and species **2** is the model system of Cpd I.

reactivity, we have also modelled several monomeric $Fe^{IV}=O$ units from species **4** $[(X)Fe^{IV}(O)(Por^{\bullet+})]^n$ {X = N **4a** ($n = -2$), NH **4b** ($n = -1$) and NH_2 **4c** ($n = 0$)} and studied their ability to activate methane.

Computational details

All calculations were performed using the Gaussian 09 suite of programs.[63] The geometries were optimised using the B3LYP-D2 functional, incorporating the dispersion correction proposed by Grimme *et al.*[64] This functional was employed by our group and others earlier to predict correct spin-state energetics of several mononuclear metal–oxo/hydroxo/superoxo complexes.[16,43,65–72] We used two different basis sets; LanL2DZ, which encompasses a double-ζ quality basis set with the Los Alamos effective core potential for Fe, and a 6-31G basis set for the other atoms (C, H, N, O, and Cl).[73,74] A single-point calculation was performed using the TZVP basis set for all the atoms.[75] A frequency calculation on the optimised structures (visualised in Chemcraft[76]) was performed to confirm the minima on the potential-energy surface (PES) and also to obtain free-energy corrections. The quoted DFT energies are B3LYP-D2 solvation energy, including free energy corrections from the frequency calculations at a temperature of 298.15 K. The solvation of the structures and energetics were studied at the B3LYP-D2 level using the polarisable continuum solvent (PCM) model using acetonitrile as the solvent.[77] Additionally, we tested the ground state of all complexes using the B3LYP-D3 level, which is not altered and found to have minor changes in the energies for the complexes (see Table S1 in the ESI†). To calculate J values, we used the gas-phase energies of the high spin and low spin states at the B3LYP-D2/TZVP level of theory. The J values were computed from the energy differences between the high spin (E_{HS}) state calculated using single determinant wave functions and the low spin (E_{BS}) state determined using the broken symmetry (BS) approach developed by Noodleman.[78,79] A negative value indicates the antiferromagnetic interactions, and a positive value indicates the ferromagnetic interactions between two centres. In the following notation $^M1$ (sFe1, sFe2), superscript 'M' denotes the total multiplicities of the spin-coupled dimer and subscript '(sFe1, sFe2)' denotes the spin multiplicity on Fe(1) and Fe(2) atoms, which are employed throughout the manuscript. We also performed DLPNO–CCSD(T) calculations using the ORCA 4.2.1 program package.[80] Here, the optimized structure coordinates from DFT were used to perform single-point gas-phase DLPNO–CCSD(T) calculations with the Dunning *et al.* correlation-consistent cc-PVTZ basis set for all atoms and we employed TIGHTPNO criteria and RIJCOSX approximation in our calculations.[81–83]

Results and discussion

We begin our investigation with four species, **1**, **2**, **3**, and **4**, exhibiting a drastic variation in their reactivity. Between **1** and **2**, species **2** is a model system of Cpd I (note the variation in the axial group –SH *vs.* –OH) and is known to activate C–H bonds such as those of norbornene,[84,85] DHA, Xanthene, *etc.*, and **1** is also a model system of Cpd II, which reacts much slower towards these substrates.[23] Of the above species, complex **4** activates methane to methanol under ambient conditions with relatively high turnover numbers, while species **3** is unreactive towards methane and even other substrates with weaker C–H bonds. Despite all of them possessing a terminal $Fe^{IV}=O$ group, their reactivities drastically depend on the nature of the axial group (–OH for **1** and **2**, [(Por)(m-CBA) $Fe^{IV}(\mu$-X)] with X = O, N for **3** and **4**, respectively) and the presence/absence of $^{\bullet+}$ character at the porphyrin ring. To fully understand their reactivity pattern, we first analysed their electronic structure and later probed their catalytic ability with an extremely inert substrate namely methane.

Electronic structures and spin-state energetics of complexes 1–4

All four iron(IV)–oxo complexes have slightly distorted octahedral geometries with an {FeN$_4$O$_2$}/{FeN$_5$O} core. For complexes **1** (the model system of Cpd II), **2** (the model system of Cpd I), and **3/4**, there are 3 (S = 0, 1, and 2), 5 (S = two 1/2, two 3/2 and 5/2), and 7 (S = 1/2, two 3/2, two 5/2, 7/2 and 9/2) spin states, respectively possible, and we have computed them all. Complexes **1**, **2**, **3**, and **4** have $S = 1$, $S = 3/2$, $S = 1/2$, and $S = 1/2$, respectively, as their ground states (see Table 1), and this is followed by higher excited states, as shown in Table 1. For complex **2**, the ground state is characterised by the intermediate spin $S = 1$ Fe centre ferromagnetically (estimated $J = +34.2$ cm^{-1} in $\hat{H} = -JS_1 \cdot S_2$ formalism) coupled to the radical in the porphyrin ring, which is also corroborated with the experimental data.[56,86–88] While for **3**, the coupling is found to be antiferromagnetic ($J = -201$ cm^{-1}). For complex **4**, it was estab-

**Table 1** The different possible spin states and the respective relative energies of complexes 1–4 and 4a–4c

Spin states	R. E. (in kJ mol^{-1})	Spin states	R. E. (in kJ mol^{-1})
1		**4**	
$^5\mathbf{1}_{(hs)}$	38.6	$^6\mathbf{4}_{(is, is)}$	19.3
$^3\mathbf{1}_{(is)}$	0.0	$^2\mathbf{4}_{(is, is)}$	46.9
$^1\mathbf{1}_{(ls)}$	121.4	**4a**	
2		$^6\mathbf{4a}_{(hs)}$	0.0
$^6\mathbf{2}_{(hs)}$	26.1	$^4\mathbf{4a}_{(hs)}$	26.9
$^4\mathbf{2}_{(hs)}$	27.3	$^4\mathbf{4a}_{(is)}$	12.2
$^4\mathbf{2}_{(is)}$	0.0	$^2\mathbf{4a}_{(is)}$	4.9
$^2\mathbf{2}_{(is)}$	6.8	$^2\mathbf{4a}_{(ls)}$	52.6
$^2\mathbf{2}_{(ls)}$	7.9	**4b**	
3		$^6\mathbf{4b}_{(hs)}$	122.3
$^{10}\mathbf{3}_{(hs, hs)}$	101.1	$^4\mathbf{4b}_{(hs)}$	38.3
$^8\mathbf{3}_{(hs, hs)}$	104.5	$^4\mathbf{4b}_{(is)}$	0.0
$^2\mathbf{3}_{(hs, hs)}$	107.6	$^2\mathbf{4b}_{(is)}$	99.4
$^6\mathbf{3}_{(is, is)}$	3.1	$^2\mathbf{4b}_{(ls)}$	44.1
$^4\mathbf{3}_{(is, is)}$	5.4	**4c**	
$^2\mathbf{3}_{(is, is)}$	0.0	$^6\mathbf{4c}_{(hs)}$	48.1
4		$^4\mathbf{4c}_{(hs)}$	46.1
$^{10}\mathbf{4}_{(hs, hs)}$	472.5	$^4\mathbf{4c}_{(is)}$	1.9
$^8\mathbf{4}_{(hs, hs)}$	250.1	$^2\mathbf{4c}_{(is)}$	0.0
$^2\mathbf{4}_{(hs, hs)}$	0.0	$^2\mathbf{4c}_{(ls)}$	35.9

lished earlier that high-spin $S = 2$ is the ground state with the Fe centres antiferromagnetically ($J = -225$ cm^{-1}) coupled to the radical centre located on the ligands, which is broadly matching with experimental data.[45,56]

The optimised structures and spin density plots of the ground state of $^3\mathbf{1}_{(is)}$, $^4\mathbf{2}_{(is)}$, $^2\mathbf{3}_{(is, is)}$, and $^2\mathbf{4}_{(hs, hs)}$ are shown in Fig. 1a–h. We have also performed DLPNO–CCSD(T) calculations on species $\mathbf{1}$ and $\mathbf{2}$ to ascertain the ground state configuration using DFT geometries. These calculations also yield $^3\mathbf{1}_{(is)}$ and $^4\mathbf{2}_{(is)}$ as the ground states, which is consistent with the DFT methods, offering confidence in the methodology employed (see Table S2 in the ESI†).[24,89–94] We would like to note here that both the employed functional in DFT and the DLPNO–CCSD(T) methods have expected error bars in the range of ~20 kJ mol^{-1}.[95] Consequently, the calculated bond lengths of the metal-ligand and spin state energetics vary with the DFT functional.[43,96–101] The energetics have traditionally been computed using DFT methods for iron–oxo species, but recently, several *ab initio* methods, including CASSCF/NEVPT2 and DLPNO–CCSD(T), have been gaining popularity for their numerically superior results, although they have their limitations in terms of active space and model size.[95,102–109] The computed bond lengths for the ground state in Fe^{IV}($\mathbf{1}$)=O were found to lie in the range of 1.656 to 1.699 Å, with the shortest bond being found for $\mathbf{3}$ and the longest for $\mathbf{1}$, and these results are consistent with earlier reports (see Tables S7,

S9 and S13 in the ESI† for spin density values).[43,45,110–113] All the Fe^{IV}=O centres in $\mathbf{1}$–$\mathbf{3}$ are found to have the $(d_{xy})^2$ $(d_{xz})^1$ $(d_{yz})^1$ $(d_{x^2-y^2})^0$ $(d_{z^2})^0$ electronic configuration with differing gaps between the orbitals (see Fig. S1–3 in the ESI† for the Eigenvalue plot of $\mathbf{1}$–$\mathbf{3}$) while $\mathbf{4}$ has a high-spin ground state having the $(d_{xy})^1$ $(d_{xz})^1$ $(d_{yz})^1$ $(d_{x^2-y^2})^1$ $(d_{z^2})^0$ configuration. In the six-coordinated Fe^{IV}=O species, the high spin ($S = 2$) state is more reactive towards C–H bond activation than the intermediate spin ($S = 1$) state.[114–116]

To assess and understand the reason for the high-spin ground state in the case of $\mathbf{4}$ compared to $\mathbf{1}$–$\mathbf{3}$, we performed further calculations on the models of complex $\mathbf{4}$, wherein the axial group [(Por)(*m*-CBA)Fe^{IV}(μ-N)] is simply modelled as N ($\mathbf{4a}$), NH ($\mathbf{4b}$) and NH$_2$ ($\mathbf{4c}$) (see Scheme 1). For model $\mathbf{4a}$, a high-spin state $^6\mathbf{4a}_{(hs)}$ state is found to be the ground state, while $^4\mathbf{4a}_{(hs)}$, $^4\mathbf{4a}_{(is)}$, $^2\mathbf{4a}_{(is)}$ and $^2\mathbf{4a}_{(ls)}$ states are higher by 26.9, 12.2, 4.9 and 52.6 kJ mol^{-1}, respectively. It was found that the intermediate spin state $^4\mathbf{4b}_{(is)}$ is the ground state for model $\mathbf{4b}$, as compared to the $^6\mathbf{4b}_{(hs)}$, $^4\mathbf{4b}_{(hs)}$, $^2\mathbf{4b}_{(is)}$, and $^2\mathbf{4b}_{(ls)}$ states which are higher by 122.3, 38.3, 99.4 and 44.1 kJ mol^{-1}, respectively. The ground state in model $\mathbf{4c}$ is also an intermediate spin state $^2\mathbf{4c}_{(is)}$, whereas the states $^4\mathbf{4c}_{(hs)}$, $^4\mathbf{4c}_{(hs)}$, $^4\mathbf{4c}_{(is)}$, and $^2\mathbf{4c}_{(ls)}$ are higher by 48.1, 46.1, 1.9, and 35.9 kJ mol^{-1}, respectively. The DLPNO–CCSD(T) calculations also yield $^6\mathbf{4a}_{(hs)}$, $^4\mathbf{4b}_{(is)}$, and $^2\mathbf{4c}_{(is)}$ as the ground states, which is consistent with the DFT methods (see Fig. S4, S5–S7† for the
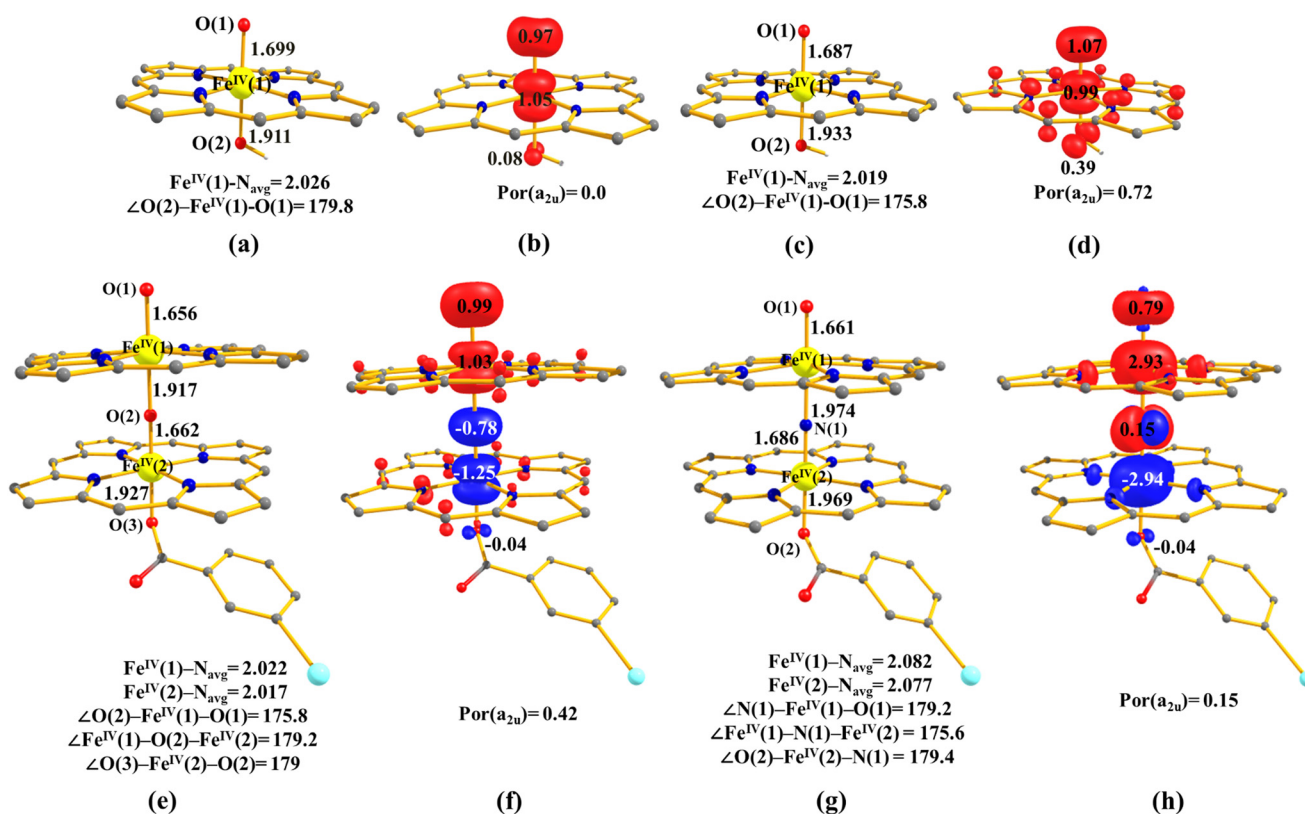

Fig. 1 The optimized structures and their corresponding spin density plots for (a and b) $^3\mathbf{1}_{(is)}$, (c and d) $^4\mathbf{2}_{(is)}$, (e and f) $^2\mathbf{3}_{(is, is)}$ and (g and h) $^2\mathbf{4}_{(hs, hs)}$. All the distances are given in Å and angles in °. All hydrogen atoms are omitted for clarity.

Eigen-value for the ground state and Table S2 in the ESI†). This illustrates the importance of the deprotonated N atom at the axial position in stabilizing the high-spin state. The switch from a high-spin to an intermediate spin is dictated by the $\Delta(E_{\pi^*xz} - E_{\sigma^*x^2-y^2})$ gap. Careful analysis of the Eigen-value plot of **4**, and **4a–c** reveals that the energy of the $\sigma^*_{x^2-y^2}$ orbital remains unaltered for all four species while the π^*_{xz} orbital is altered (see Fig. S5, S8, and S9†). Particularly for **4**, and **4a**, the axial nitrogen atom is involved in the π-bonding, leading to the destabilization of these orbitals and the reduction of the $\Delta(E_{\pi^*xz} - E_{\sigma^*x^2-y^2})$ gap (see Fig. S10†). Protonation of the nitrogen atom weakens the π-bonding capability leading to larger $\Delta(E_{\pi^*xz} - E_{\sigma^*x^2-y^2})$ and hence the stabilization of the intermediate spin as the ground state. As we move from **4** to **4c**, it is clear that the Fe^{IV}–N_{ax} bond length increases, reflecting the stronger Fe^{IV}=N π character in **4**, followed by **4a**, **4b**, and **4c**. Also, the length of the $Fe^{IV}(1)$=O1 bond decreases when we move from **4** to **4c**. It is clearly suggested that the $Fe^{IV}(1)$=O1 bond lengths increase with a decrease in the $Fe^{IV}(1)$–N_{ax} bond lengths (see Table S3 in the ESI†). The elongation of the $Fe^{IV}(1)$=O1 bond length is likely to generate a greater oxyl radical character[117] and is expected to increase the catalytic activity of these species towards the C–H bond of methane. The computed spin density values on the $Fe^{IV}(1)$, O1, N1, and a_{2u} orbitals are found to be 3.01/3.04/2.96, 0.78/0.87/0.72, 1.81/0.86/0.82, and −0.61/0.26/0.55, for **4a**/**4b**/**4c**, respectively. Our calculations reveal a significant radical character on the porphyrin ring in the case of **2**, a slightly reduced spin density in the case of **3**, and much lower spin densities for **4a** and **4c**. For **4b**, **4**, and **1**, only very little spin density is detected at the porphyrin ring. As **1** (the model system of Cpd II) is not a formal radical species, detection of similar spin density for **4b** and **4** (on the porphyrin attached to the Fe^{IV}=O unit) suggests that they are not true cation radical species as assumed (see Table S4 in the ESI†).

The relationship between the internuclear distance and force constant has been proposed by Badgers,[118] and this has been widely used to explain the axial ligand effect of Cpd I and related models.[110,119] We have also employed the same for our systems, and the plot is shown in Fig. 2. Although our complexes are not strictly simple axial ligand substituents, as demonstrated by Visser and Green in other examples,[110,119] we still see a near-linear correlation suggesting that Badger's rule is applied even when dinuclear systems such as complexes **3** and **4** are considered as a mononuclear counterpart with different nuclearity being the axial ligand effect. Furthermore, the bond length variation in Fe–O affirms that all the cases studied are true iron(IV)–oxo units.[119]

Reactivity of 1 and 2 towards methane

The mechanism adopted for methane activation by **1–4** is shown in Scheme 2. In the generic mechanism adopted here, the Fe^{IV}=O species are expected to activate the C–H bond in the first step via **ts1**, leading to the formation of a radical intermediate (**int1**). In the subsequent step, –OH rebound via **ts2** is assumed, leading to the hydroxylated product (**P**) and the Fe^{II}
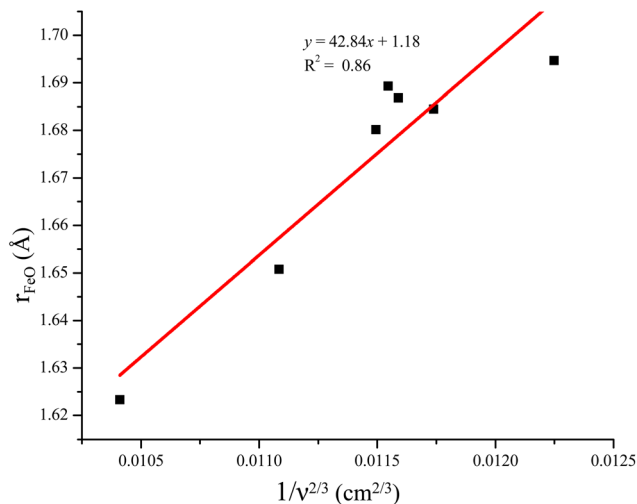

Fig. 2 Badger plot for the Fe−O bond length *versus* $1/\nu_{FeO}^{2/3}$ (cm$^{2/3}$) with the ν_{FeO} stretching vibration for the Fe−O bond from Scheme 1. Here, we have used only high-spin optimized structures for our calculations.

precursor. This mechanism is based on the experimental pieces of evidence gathered for the reactivity of Fe^{IV}=O species and cytochrome P450.[92,120]

To further understand the reactivity pattern between these four complexes, we have calculated the barrier height for the C–H bond activation of methane using these complexes. For species **1**, the **1**-^{3}**R**$_{(is)}$ state is found to be the ground state, followed by the **1**-^{5}**R**$_{(hs)}$ and **1**-^{1}**R**$_{(ls)}$ states with an energy margin of 38.6 and 121.4 kJ mol^{-1} higher in energy, and these two different spin states ($S = 2$, and 0) of the Fe^{IV}–oxo species may participate in the hydroxylation process. The calculated barrier height for the **1**-^{3}**ts1**$_{(is)}$ transition state is 108.4 kJ mol^{-1} (155.2 and 233.8 kJ mol^{-1} for the **1**-^{5}**ts1**$_{(hs)}$ and **1**-^{1}**ts1**$_{(ls)}$ species, respectively, see Fig. 3, 4a and Tables S5, S6 in the ESI†). A similar model system of Cpd II has been reported by several groups, whereas –SH, –His, –Cl, and –NCCH$_3$ groups are present as axial ligands instead of the –OH group. In all cases, the $S = 1$ state was found to be the ground state. The calculated structural parameters were also found to be almost identical to those reported with different axial ligands, as mentioned above. The calculated barrier height is also found to be similar to that for species **1**.[24,53,121,122] The Fe(1)–O(1)–H bond angle calculated for **1**-^{3}**ts1**$_{(is)}$ is found to be 114°, suggesting a π-pathway due to a β-electron transfer from the σ_{CH} bond (see Table S7 for spin densities in the ESI and see Fig. S11 in the ESI†).[123] The analysis of spin densities and charges suggests that the mechanism favours the radical pathway of the C–H bond at the transition state (see Fig. 4b and Table S7 in the ESI† for other states).

In the next step, the H-atom abstraction leads to the exothermic formation of Fe^{III}–OH and methyl radical intermediate species (**1-int1**), where **1**-^{3}**int1**$_{(ls)}$ is the ground state, followed by **1**-^{7}**int1**$_{(hs)}$, **1**-^{5}**int1**$_{(hs)}$, **1**-^{5}**int1**$_{(is)}$, **1**-^{3}**int1**$_{(is)}$, **1**-^{1}**int1**$_{(ls)}$ states at 110.6, 111.3, 130.8, 131.9 and 91.3 kJ mol^{-1} higher in energy, respectively (see Fig. 4c and d for bond
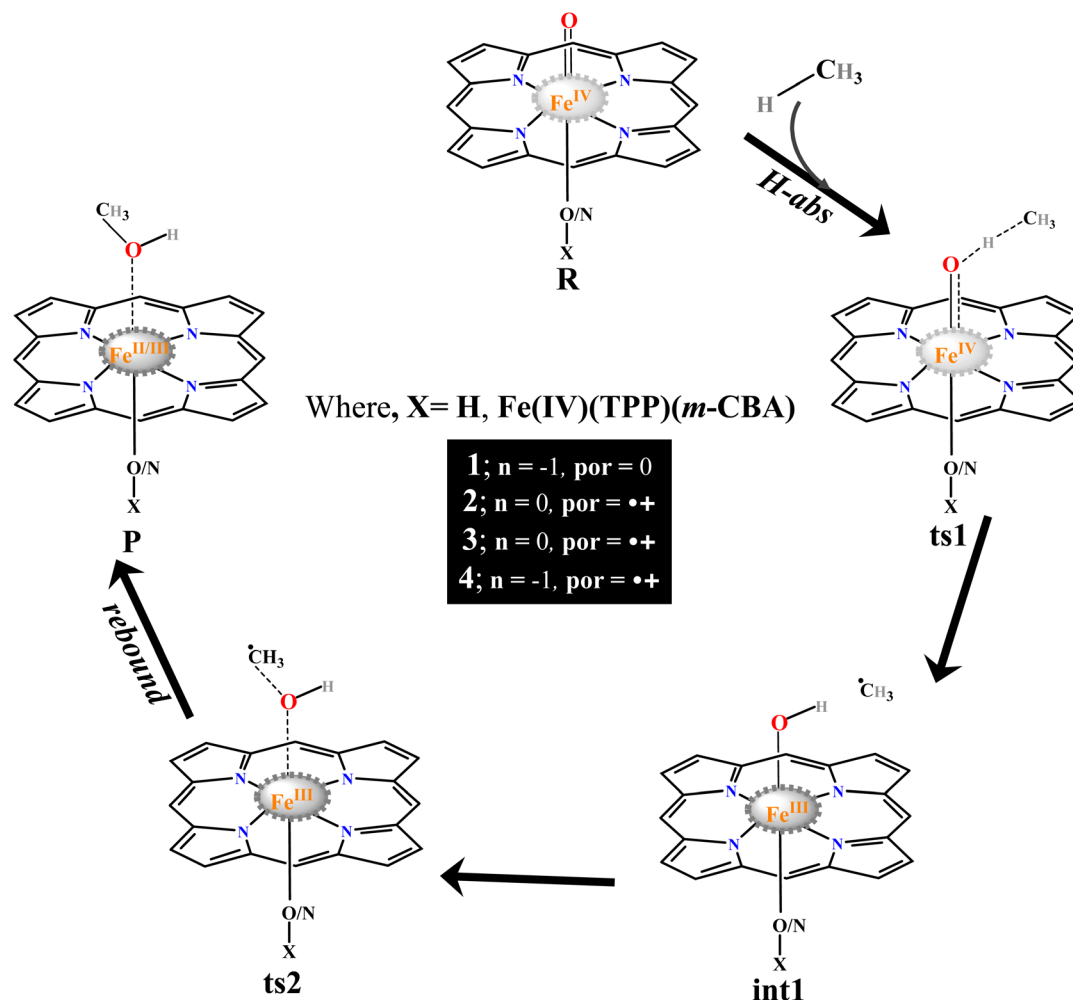
Scheme 2 The schematic mechanism proposed for the C−H bond activation of methane by the Fe(ɪᴠ)−oxo unit. Species **1** is the model system of Cpd II and species **2** is the model system of Cpd I.

length and spin density, respectively). In the radical rebound step, the $Fe^{III}(1)-O(1)H$ and methyl radicals recombine to give methanol as a product. Here, we have also computed six possible spin states, where the **1**-^{1}**ts2**$_{(ls)}$ species is found to be at 43.9 kJ mol^{-1}, followed by **1**-^{7}**ts2**$_{(hs)}$ (74.6 kJ mol^{-1}), **1**-^{5}**ts2**$_{(hs)}$ (51.0 kJ mol^{-1}), **1**-^{5}**ts2**$_{(is)}$ (76.3 kJ mol^{-1}), **1**-^{3}**ts2**$_{(is)}$ (80.8 kJ mol^{-1}), **1**-^{3}**ts2**$_{(ls)}$ (56.1 kJ mol^{-1}) transition states from the **1**-^{3}**int1**$_{(ls)}$ state. For the **1**-^{1}**ts2**$_{(ls)}$ transition state, the $Fe^{III}(1)-O(1)H$ bond is further elongated (1.913 Å) compared to the intermediate, and at the same time, the newly formed $O(1)-C$ bond is shortened by 2.230 Å than that of the intermediate (see Fig. 4e and c as well as Table S6 in the ESI† for other states). At the **1**-^{1}**ts2**$_{(ls)}$ state, the $Fe(1)-O(1)-C$ bond angle is determined to be 118°, while the $Fe^{IV}(1)-O(1)-H$ angle is also determined to be 114°, suggesting that both steps occur in the π-channel. In addition, here, the **1**-^{1}**ts2**$_{(ls)}$ state is significantly higher than **1**-^{3}**ts1**$_{(is)}$, suggesting that the rate-determining step is a rebound step over the HAT step. In the last step, the $-O(1)H$ group is expected to rebound to the methyl radical to give methanol (**1**-**P**). Here, we have computed three possible spin

states with **1**-^{5}**P**$_{(hs)}$ lying at −90.8 kJ mol^{-1}, indicating the exothermic formation of this product (see Fig. 3 for the energetics of other spin states and Fig. 4g and h for the optimised and spin density plots of the ground state).

The energy profile for the C–H activation of methane with $[(OH)(Por^{•+})Fe^{IV}=O]$ is shown in Fig. 5. For species **2** (**2**-**R**), the **2**-^{4}**R**$_{(is)}$ state is found to be the ground state, followed by the **2**-^{6}**R**$_{(hs)}$, **2**-^{4}**R**$_{(hs)}$, **2**-^{2}**R**$_{(is)}$, and **2**-^{2}**R**$_{(ls)}$ states with an energy margin of 26.1, 27.3, 6.8 and 7.9 kJ mol^{-1}, respectively, higher in energy. The calculated barrier height for the C–H activation of methane is estimated to be 67.6 kJ mol^{-1} from the reactant, followed by the **2**-^{4}**ts1**$_{(is)}$, **2**-^{2}**ts1**$_{(ls)}$, **2**-^{4}**ts1**$_{(hs)}$, and **2**-^{6}**ts1**$_{(hs)}$ spin states with an increasing energy order of 92.4, 107.6, 131.9, and 138.6 kJ mol^{-1}, respectively from the **2**-^{4}**R**$_{(is)}$ state (see Fig. 5). The calculations reveal that the reactions of **2** proceed by two-state reactivity (TSR) or multi-state reactivity (MSR), which involves **2**-^{4}**ts1**$_{(is)}$ and **2**-^{2}**ts1**$_{(is)}$ states that together determine the rate of the reaction. The $Fe(1)-O(1)-H$ bond angle at **2**-^{2}**ts1**$_{(is)}$ is 113°, and the MO and spin density analyses indicate that an α-electron is transferred to the a_{2u} orbital of the
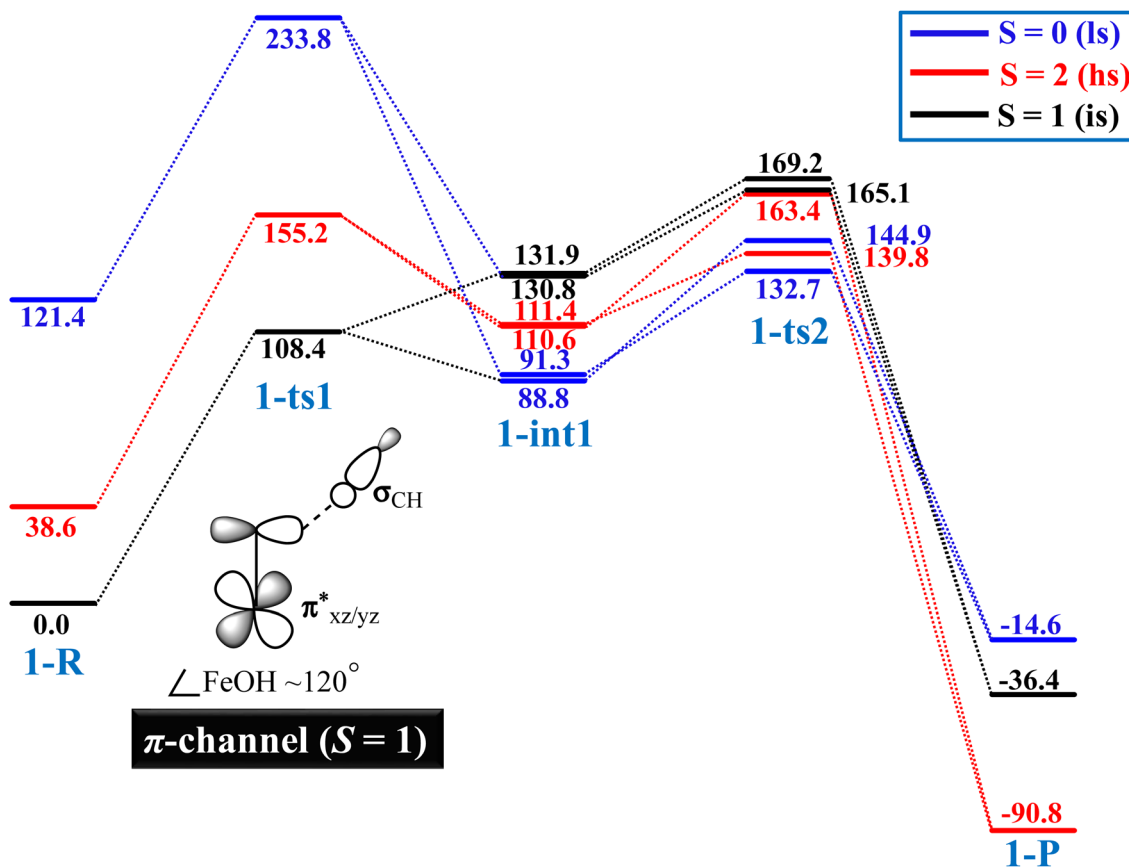
Fig. 3 B3LYP-D2 computed potential energy surface for the C–H bond activation of methane by species **1** (kJ mol^{-1}).

porphyrin ligand and not to the Fe centre, maximizing the exchange-enhanced reactivity (see Fig. S12b in the ESI†) as witnessed for the Cpd I mimics.[92,124,125] Spin density analysis reveals that migrating hydrogen has a positive spin density, whereas the other two groups, which flank this hydrogen, have a negative spin density (see Fig. 6 and Table S10† for other states). For **2-^{4}ts1$_{(is)}$**, two transition states are computed, with one following the π-channel (92.4 kJ mol^{-1}) and the other following the δ-channel (79.9 kJ mol^{-1}), and both have an α-electron transferred from σ$_{CH}$ to a$_{2u}$ and σ*$_{x^2-y^2}$ orbitals, respectively. These characteristics of these two transition states reveal the importance of spin states in understanding these intricate reaction mechanisms.[126] The calculated barrier height for the C–H bond activation of methane varies slightly with different axial groups as reported by several other groups described above using the same level of theory.[21,87,90,103,104]

In the next step, a hydrogen atom abstraction leads to the endothermic formation of a Fe^{IV}(1)–OH and methyl radical intermediate[127] (**2-int1**), with the **2-^{4}int1$_{(is)}$** state being found to be the lowest-lying at 45.0 kJ mol^{-1} (see Fig. 5) followed by **2-^{6}int1$_{(hs)}$**, **2-^{4}int1$_{(hs)}$**, **2-^{2}int1$_{(is)}$**, and **2-^{2}int1$_{(ls)}$** states at 102.3, 127.4, 45.6, and 86.0 kJ mol^{-1}, respectively higher in energy (see Fig. 6c). The **2-^{4}int1$_{(is)}$** state has shorter Fe(1)–O1(H) bonds than **1-^{3}int1$_{(ls)}$** (1.799 vs. 1.891 Å and 45.0 vs. 88.8 kJ mol^{-1}, respectively), and this is one of the driving forces for

relatively small barriers computed.[128,129] The calculated rebound barrier height for this **2-^{2}ts2$_{(is)}$** state is found to be 2.3 kJ mol^{-1} from the intermediate species, followed by **2-^{6}ts2$_{(hs)}$**, **2-^{4}ts2$_{(hs)}$**, **2-^{4}ts2$_{(is)}$**, and **2-^{2}ts2$_{(ls)}$** states at 63.9, 130.6, 49.8, and 8.8 kJ mol^{-1}, respectively higher in energy. Our calculation suggests that the two transition states **2-^{2}ts2$_{(is)}$** and **2-^{4}ts2$_{(is)}$** remain degenerate up to the radical-rebound step and we found no exchange enhancement (see Fig. 6e and Table S9 in the ESI† for other states). Interestingly, the **2-^{2}ts2$_{(is)}$** state is significantly lower than the **2-^{2}ts1$_{(is)}$** state, suggesting HAT as a rate-determining step over the rebound step. Here, we have computed three possible spin states with **2-^{5}P$_{(hs)}$** lying at −196.7 kJ mol^{-1} from the reactant. The thermodynamic formation of this product is estimated to be −244.0 kJ mol^{-1}, indicating the facile formation compared to species **1** (see Fig. 5 for the energetics of other spin states and Fig. 6g and h for the optimised, and spin density plots of the ground state). The overall calculated barrier height suggests that species **2** is much more reactive than species **1**, which is also confirmed by experimental data.[23]

Reactivity of 3 towards methane

To construct the potential energy surface (PES) for methane hydroxylation, we calculated all possible spin states for species **3**, as shown in the above scheme (see Fig. 7). The calculated barrier height for the **3-^{2}ts1$_{(is, is)}$** state is found to be 113.4 kJ
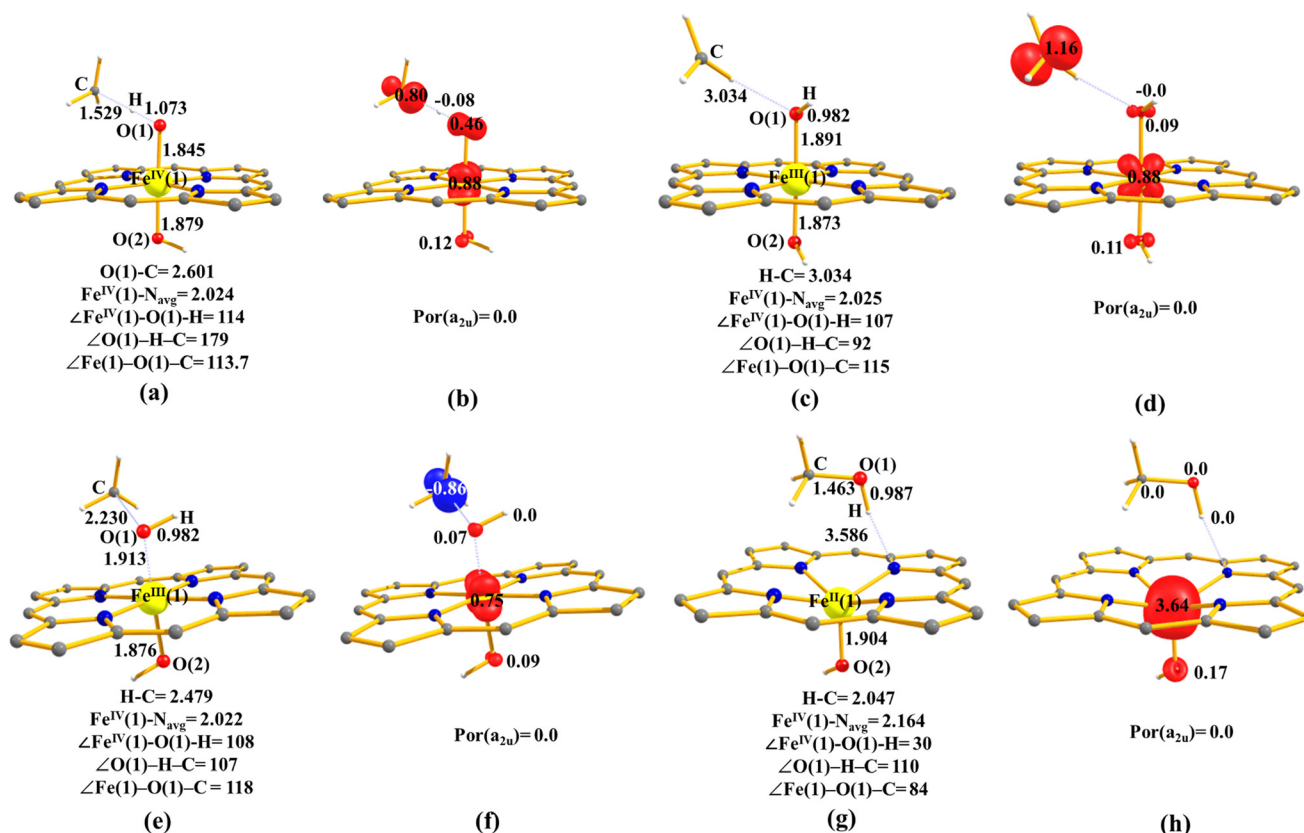
Fig. 4 The optimized structures and their corresponding spin density plots for (a and b) **1**-^{3}**ts1**$_{(is)}$, (c and d) **1**-^{3}**int1**$_{(ls)}$, (e and f) **1**-^{1}**ts2**$_{(ls)}$ and (g and h) **1**-^{5}**P**$_{(hs)}$. All the distances are given in Å and angles in °. All hydrogen atoms (except CH$_4$) are omitted for clarity.

mol^{-1} from the reactant (Fig. 8a and b) with five other transition states **3**-^{10}**ts1**$_{(hs, hs)}$, **3**-^{8}**ts1**$_{(hs, hs)}$, **3**-^{2}**ts1**$_{(hs, hs)}$, **3**-^{8}**ts1**$_{(is, is)}$, and **3**-^{4}**ts1**$_{(is, is)}$ being expected to lie higher at the energy margins of 116.2, 117.2, 227.1, 232.7, and 239.2 kJ mol^{-1}, respectively compared to the **3**-^{2}**R**$_{(is, is)}$ state. The computed bond lengths for the ground state of the transition state **3**-^{2}**ts1**$_{(is, is)}$ are shown in Fig. 8a. As the H–C bond is broken at the transition state, this subsequently spurs the generation of radical character at the carbon atom, suggesting a HAT type of reaction (as observed by the spin density values on the C atom of the methyl group and see Fig. 8b).[130] The computed ∠Fe(1)–O(1)⋯H angle is estimated to be 114.2°, suggesting a π-type pathway for the hydrogen atom abstraction reaction from methane.[131] The orbital evolution diagram for the C–H bond activation of **3**-^{2}**ts1**$_{(is, is)}$ is shown in Fig. 9. This represents an orbital-controlled reactivity, which operates because the intermediate-spin state is exchange-saturated.[131] This transition state has a significant barrier compared to species **1** and **2**, and this is primarily due to the orbital-controlled nature of the reaction and the strong destabilisation of high-spin Fe^{IV} states due to a stronger ligand field, and this closes the possibility of spin-crossover states' involvement in the reactivity. Another important point to note here is that a β-electron is transferred from the substrate to the Fe^{IV} centre and not into the a$_{2u}$ orbital during the transition state **3**-^{2}**ts1**$_{(is, is)}$.

In the next step, after hydrogen abstraction of the methane molecule, the Fe^{III}(1)–O(1)H and methyl radical intermediates form (**3**-**int1**). We have computed all possible spin states, namely; **3**-^{12}**int1**$_{(hs, hs)}$, **3**-^{10}**int1**$_{(hs, hs)}$, **3**-^{4}**int1**$_{(hs, hs)}$, **3**-^{2}**int1**$_{(hs, hs)}$, **3**-^{8}**int1**$_{(is, is)}$, **3**-^{6}**int1**$_{(is, is)}$, **3**-^{4}**int1**$_{(is, is)}$, and **3**-^{2}**int1**$_{(is, is)}$. Here, the **3**-^{2}**int1**$_{(is, is)}$ state is found to be low lying with just 90.0 kJ mol^{-1} lower than the transition state **3**-^{2}**ts1**$_{(is, is)}$, revealing the endothermic nature of the reaction. Other intermediates are computed to be much higher in energy with the **3**-^{12}**int1**$_{(hs, hs)}$, **3**-^{10}**int1**$_{(hs, hs)}$, **3**-^{4}**int1**$_{(hs, hs)}$, **3**-^{2}**int1**$_{(hs, hs)}$, **3**-^{8}**int1**$_{(is, is)}$, **3**-^{6}**int1**$_{(is, is)}$, and **3**-^{4}**int1**$_{(is, is)}$ states lying 155.5, 144.8, 156.9, 161.7, 114.0, 121.4 and 109.6 kJ mol^{-1}, respectively, higher in energy from the **3**-^{2}**R**$_{(is, is)}$ state (see Fig. 7). This step was found to be endothermic in nature compared to species **1** and **2** and cytochrome P450 and sMMO enzymes, revealing resemblance in the energetic landscape despite significant structural/electronic differences.[92,132,133] The computed bond lengths and spin density plot for the ground state of the intermediate species (**3**-**int1**) are shown in Fig. 8c and d (see also Table S12a† for other states).

Following the H-abstraction, the intermediates (**3**-**int1**) undergo rebound *via* **3**-**ts2** between the Fe^{III}–OH group and the methyl radical to form methanol. Our calculations show that the **3**-^{2}**ts2**$_{(is, is)}$ state is the lowest-lying with a barrier height of 36.2 kJ mol^{-1} with respect to the intermediate species (Fig. 8e

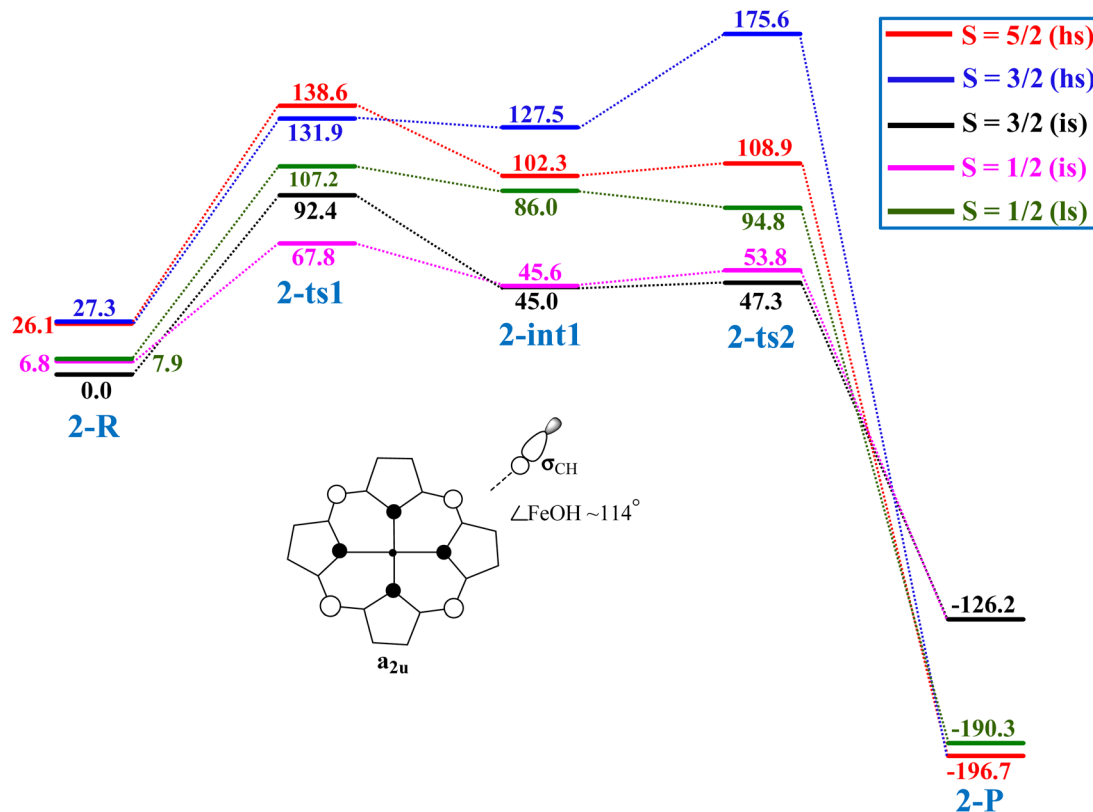**Fig. 5** B3LYP-D2 computed potential energy surface for C−H bond activation of methane by species **2** (kJ mol^{-1}).

and f), while the 3-^{12}**ts2**$_{(hs,\ hs)}$, 3-^{10}**ts2**$_{(hs,\ hs)}$, 3-^{4}**ts2**$_{(hs,\ hs)}$, 3-^{2}**ts2**$_{(hs,\ hs)}$, 3-^{8}**ts2**$_{(is,\ is)}$, 3-^{6}**ts2**$_{(is,\ is)}$, and 3-^{4}**ts2**$_{(is,\ is)}$ transition states lie higher at 65.6, 72.2, 85.1, 87.8, 61.8, 36.7, and 63.5 kJ mol^{-1}, respectively from the 3-^{2}**int1**$_{(is,\ is)}$ state (see Fig. 8e). The Fe^{IV}=O bond length remains almost similar throughout the rebound mechanism, whereas the Fe^{III}–O bond length is significantly elongated to 2.021 Å from 1.713 Å at the transition state. The computed ∠Fe–O···H bond angle is estimated to be 113.4°, suggesting a π-type pathway for the rebound mechanism. Furthermore, a β-electron is found to be transferred from methane to the a$_{2u}$ orbital of the porphyrin ring, and this is exemplified in the computed spin densities (see Table S13† for other states). The lowest barrier height for the rebound step is estimated to be 36.2 kJ mol^{-1}. Although this is not substantial compared to species **2** and **4**, this is significant (2.3 kJ mol^{-1} for **2** and barrier-less for **4**), suggesting the rate maintained for the –OH rebound if the H atom abstraction step is completed, and this is corroborated with experimental data.[52,56] This fact has also been reported by Sorokin and co-workers, showing no oxidation of CH$_4$ under experimental conditions using the diiron μ-oxo (FePc^{t}Bu$_4$)$_2$O species.[7,55] The Fe^{III}–OH and methyl radicals are expected to recombine *via* the rebound step to give methanol as a product (**3-P**) (see Fig. 8g and h). Here, we have computed four possible spin states, 3-^{10}**P**$_{(hs,\ hs)}$, 3-^{2}**P**$_{(hs,\ hs)}$, 3-^{6}**P**$_{(is,\ is)}$, and 3-^{2}**P**$_{(is,\ is)}$, where the 3-^{2}**P**$_{(is,\ is)}$ spin state is found to be the lowest-lying in energy with −142.3 kJ mol^{-1}, followed by 3-^{10}**P**$_{(hs,\ hs)}$, 3-^{2}**P**$_{(hs,}$

hs), and 3-^{6}**P**$_{(is,\ is)}$ states with energy margins of −79.4, −111.7, and −134.9 kJ mol^{-1}, respectively, indicating the less facile formation of this product.

Reactivity of 4a–4c towards methane

Furthermore, we determined the C–H bond activation barrier height of methane using species **4a–4c** (see Fig. S13†). For the **4a–4c** species, the barrier heights are calculated to be 58.4, 88.3 and 90.6 kJ mol^{-1} at the ^{4}**ts1**$_{(is)}$ surface. The other spin states (^{6}**ts1**$_{(hs)}$, ^{4}**ts1**$_{(hs)}$, ^{2}**ts1**$_{(is)}$, and ^{2}**ts1**$_{(ls)}$) were found to be at higher energies than the ^{4}**ts1**$_{(is)}$ state (see Table S14 in the ESI†). Compared to species **4**, species **4a–4c** have a higher barrier height for the C–H bond activation of methane. We have reported first the reactivity of species **4**, and this was subsequently studied in detail by other groups.[43,52] The computed bond lengths of the ground state (^{4}**ts1**$_{(is)}$) for the Fe^{IV}(1)–O(1), O(1)–H, and C–H bonds are found to be 1.873/1.844/1.751, 1.097/1.116/1.157, and 1.461/1.419/1.377 Å for species **4a/4b/4c**, respectively. From our calculations, it is evident that the longer Fe–O bond in **4a** is more reactive towards methane activation than the shorter bonds in species **4b** and **4c**. However, from **4a** to **4b**, the Fe–N(1) bond decreases significantly, whereas for **4c** the Fe–N(1) bond increases slightly compared to **4a** (see Fig. S13 in the ESI†). The Fe–O–H angle suggests that the Fe^{IV} unit accepts electrons from the σ$_{CH}$ into a π*$_{xz/yz}$ orbital, suggesting a π-channel preference over the σ and δ-channels. Our observations have shown that the Fe–O–H
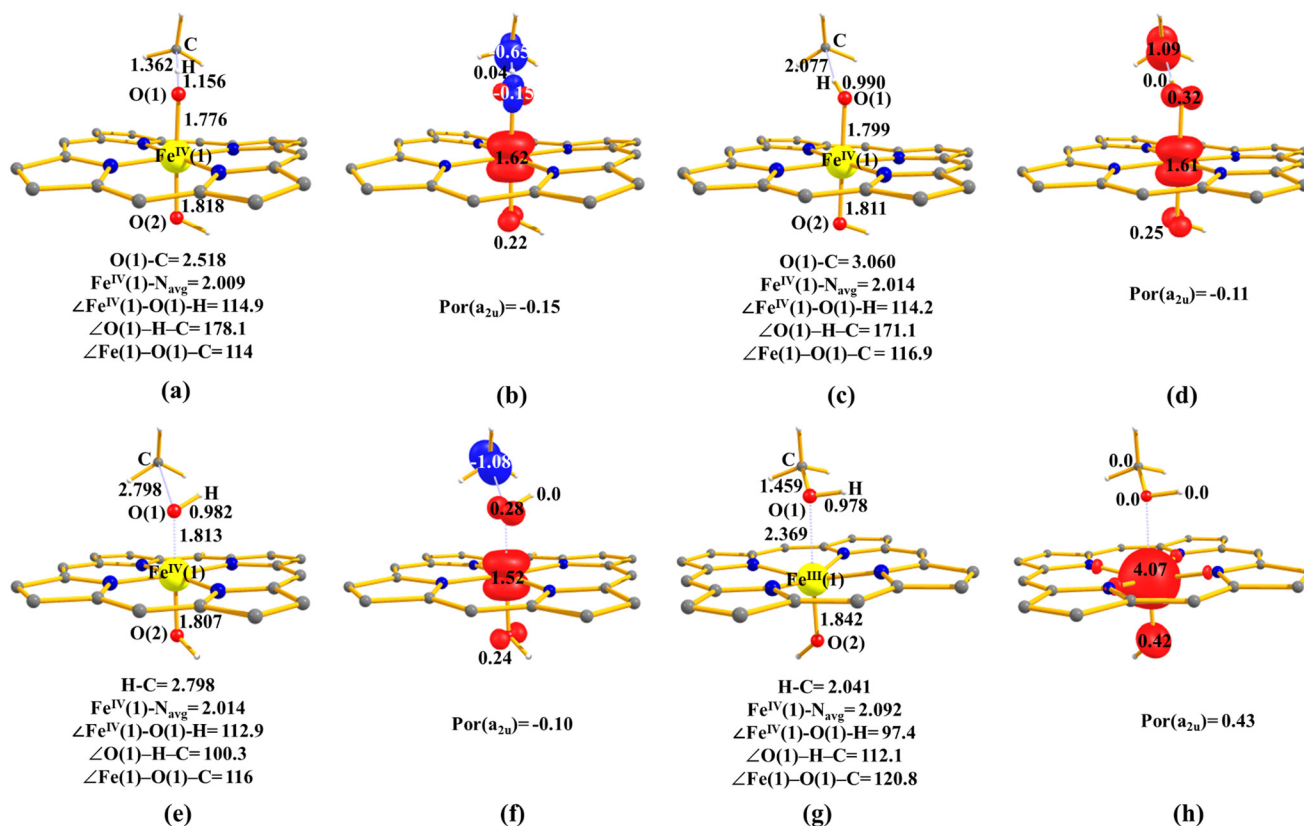
Fig. 6 The optimized structures and its corresponding spin density plots for (a and b) **2-^{2}ts1$_{(is)}$**, (c and d) **2-^{4}int1$_{(is)}$** (e and f) **2-^{2}ts2$_{(is)}$**, and (g and h) **2-^{5}P$_{(hs)}$**. All the distances are given in Å and angles in °. All hydrogen atoms (except CH$_4$) are omitted for clarity.
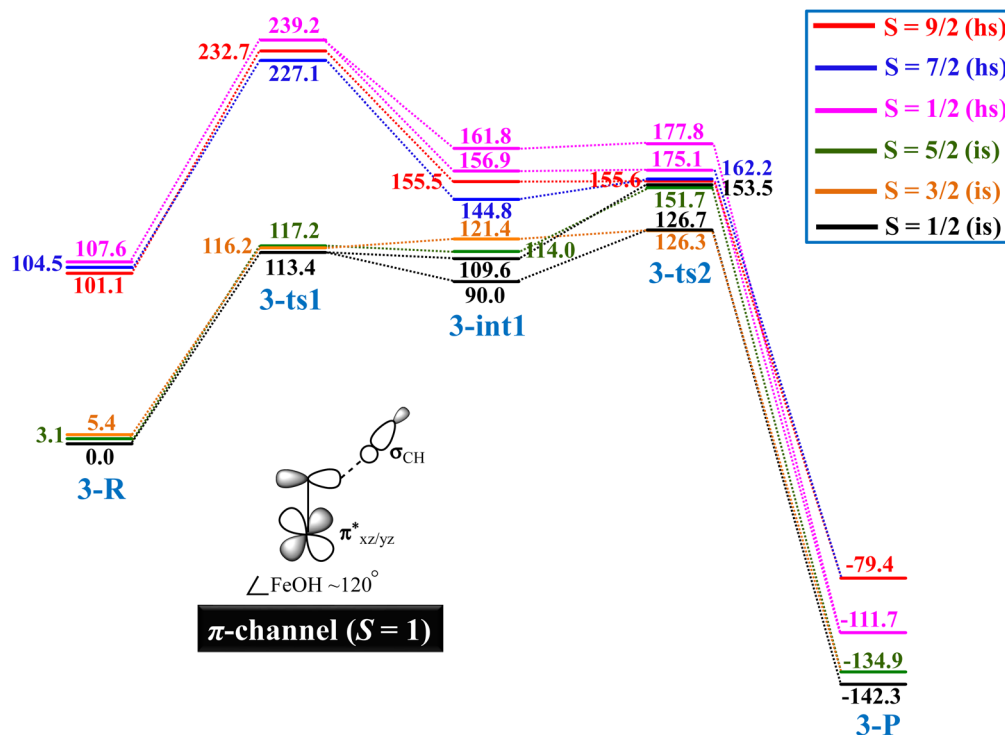
Fig. 7 B3LYP-D2 computed potential energy surface for the C–H bond activation of methane by species **3** (kJ mol^{-1}).
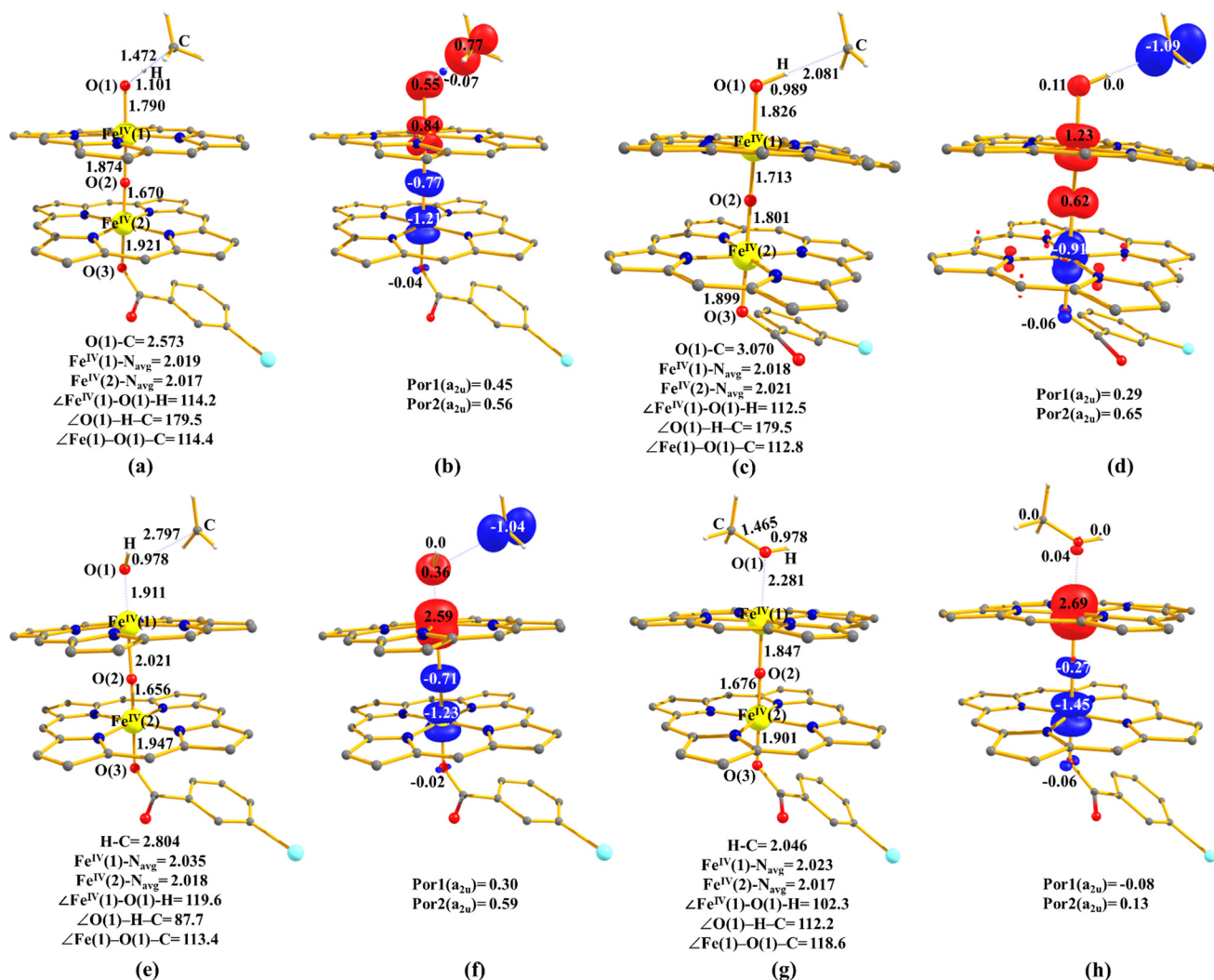
Fig. 8 The optimized structures and their corresponding spin density plots for (a and b) $3\text{-}^2\text{ts1}_{(is,\ is)}$, (c and d) $3\text{-}^2\text{int1}_{(is,\ is)}$, (e and f) $3\text{-}^2\text{ts2}_{(is,\ is)}$, and (g and h) $3\text{-}^2\text{P}_{(is,\ is)}$. All the distances are given in Å and angles in °. All hydrogen atoms (except CH_4) are omitted for clarity.
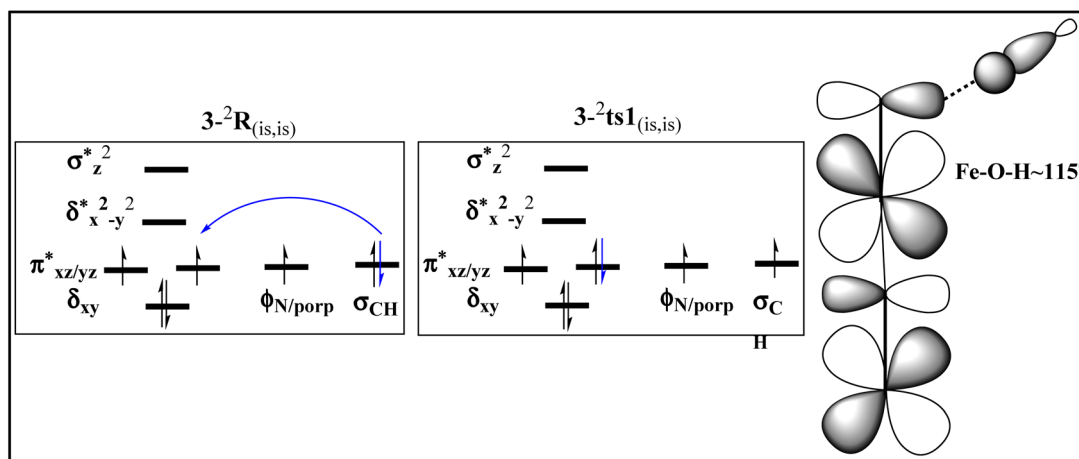
Fig. 9 The orbital evolution diagram for the C−H activation for $3\text{-}^2\text{ts1}_{(is,\ is)}$.

angle has decreased from **4** to **4c**. The steric hindrance of **4** is lower than that of **4a–4c**, *i.e.* **4** has lower C–H activation energy than **4a–4c** (see Fig. S13 in the ESI†).[45] Moving from the transition state of **4a** to **4c**, the spin density values at the iron centre increase at the same time as the radical characters of the porphyrin (a_{2u} orbital) decrease, and this is also accompanied by a drastic reduction in the spin density of the nitrogen atom N(1). This is due to the nature of the Fe–N bond and the protonation state of the N(1) atom. With an increasing number of H atoms, there is a drastic reduction in its spin density. This reduction causes a concomitant reduction in the porphyrin ring. As the Fe–N bond lengths decrease as we move from **4a** to **4c**, the spin density on the Fe atom increases.

Discussion

All four oxidants were subjected to follow a similar mechanistic pathway to methane hydroxylation, but they have different C–H bond activation barriers, as shown in Fig. 10. Firstly, we carefully looked at the deformation energy, interaction energy, and orbital mixing between the substrate and the catalyst. To assess deformation energies for the corresponding hydrogen atom abstraction, transition states are computed, and the

values are estimated to be 147.6, 124.1, 67.1, 77.5, 147.1, and 112.1 kJ mol^{-1} for **1**-^{3}**ts1**$_{(is)}$, **2**-^{2}**ts1**$_{(is)}$, **3**-^{2}**ts1**$_{(is, is)}$, **4**-^{2}**ts1**$_{(is, is)}$, **4a**-^{4}**ts1**$_{(is)}$, **4b**-^{4}**ts1**$_{(is)}$, and **4c**-^{4}**ts1**$_{(is)}$, respectively. Based on our calculations of the deformation energy, species **4** has the lowest deformation energy compared to the other six species, indicating that C–H bond activation is preferred over that of the other species. The deformation energy at the transition state contributes 40% to the barrier height for species **4**, while for species **1**, **2**, **3**, **4a**, **4b**, and **4c**, the values were estimated to be 73, 83, 91, 75, 60, and 81%, respectively. Interestingly, while deformation is a minor contributor to **4**, there are other factor contributions in the other six species that dominate the barrier height. As a result of a closer examination of the interaction energy, it is evident that in all six species, the interaction energy also contributes to the barrier height of the reaction.[134] Due to the mixing of the orbitals and favourable electrostatic interactions in **ts1**, the interaction energy is stabilized (see Table S15 in the ESI†). For the C–H bond activation observed with all species, the deformation energies are significantly larger than the barriers (see Fig. S14 in the ESI†), which indicates that all of the TSs have very large stabilizing interactions, resulting in barriers well below the energies associated with the deformation.[134] In all cases, we have found that the C–H bond activation of methane towards the Fe^{IV}=O unit pro-
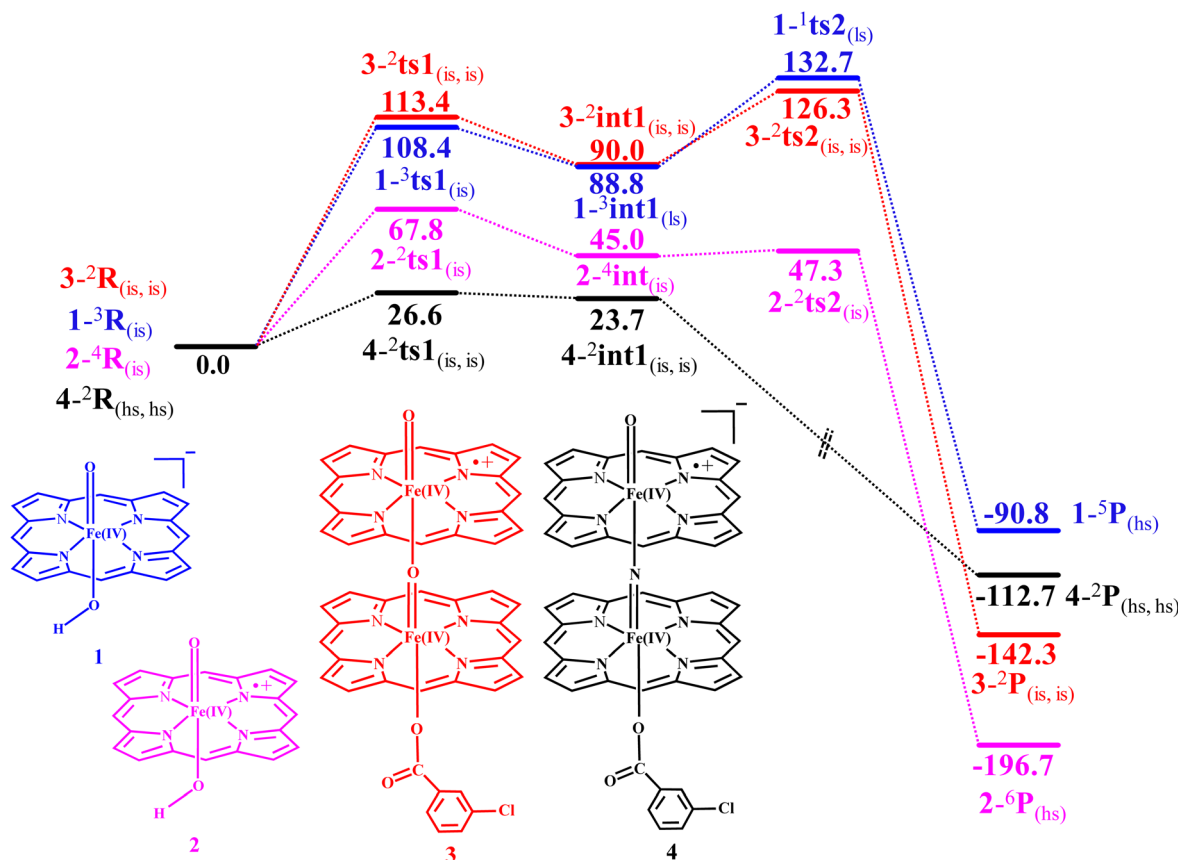

Fig. 10 Comparative potential energy surface (energies are in kJ mol^{-1}) for the C−H activation of methane by **1** (blue), **2** (magenta), **3** (red), and **4** (black) oxidants.

ceeds *via* the hydrogen atom transfer (HAT) pathway compared to the proton-coupled electron transfer (PCET) pathway.

Furthermore, we looked carefully at how the reaction channel and C–H⋯π interactions affect the barrier height of the reaction. Furthermore, all species **1–4** were found to react *via* the π-channel, unlike non-heme Fe^{IV}=O species that prefer to engage in the σ-channel with the substrate to reduce the barrier height.[71,135] In heme models, due to the presence of a flat equatorial ligand, the substrate can approach the oxo group in a π-fashion without any substantial substrate-catalyst strain, which is usually present in non-heme models. Furthermore, we have observed C–H⋯π non-covalent interactions[136–142] between the substrate and the porphyrin ring (2.60 to 3.40 Å) anchoring the substrate in the vicinity of all four species. This isosurface demonstrates that the π-face of the porphyrin ring and the edge of the methyl group engage in an attractive interaction[143] (see Fig. S15 in the ESI†). Our analysis of the C–H⋯π interaction at the HAA transition state on the triplet surface shows that there are stronger and larger ∠C–H⋯π-groups for species **2** than for species **1** and **3** (see Fig. S16 in the ESI†). Similarly, we compared the C–H⋯π interactions with species **4** and found a slightly weaker C–H⋯π interaction and smaller ∠C–H⋯π-groups than those in species **2**, and stronger interactions than with **1**, and **3**. Due to the presence of a high spin state at the iron center, species **4** is more reactive than species **2** towards methane activation, despite having a slightly weaker C–H⋯π interaction and smaller ∠C–H⋯π-groups. Furthermore, the calculated inter-

action energy for species **1** is found to be −40.7 kJ mol⁻¹. This interaction is mainly due to the electrostatic interaction energy (−37.9 kJ mol⁻¹). The rest of the energy −2.8 kJ mol⁻¹ comes from van der Waal interactions such as non-covalent interactions of C–H⋯π, exchange interactions, dispersion interactions, *etc.* contributing to a reduction of the energy barrier (see the ESI† for details). This is also supported by a previous study on the C–H⋯π interaction between coronene and methane.[144] For these reasons, for all catalysts modelled, a preferential π-pathway is noted.[43,45,140,145]

For all complexes, the π(Fe=O) orbitals are high in energy to be the source of electrons.[146] This forces the axial HO⁻ ligand to participate in the π orbitals of the HO–Fe=O moiety (see Fig. S2 in the ESI†) and thus increases the energy of all out-of-phase combinations π^*_{xz}(HO–Fe=O) and π^*_{yz}(HO–Fe=O) compared to {(Por)(*m*-CBA)Fe^{IV}N}⁻. On the other hand, the axial {(Por)(*m*-CBA)Fe^{IV}O}⁻ ligand participates in the π orbitals of the {(Por)(*m*-CBA)Fe^{IV}O–Fe=O} moiety (see Fig. S3 in the ESI†) and thus significantly increases the energy of the all out-of-phase combinations for π^*_{xz}({(Por)(*m*-CBA)Fe^{IV}O–Fe=O}) and π^*_{yz}({(Por)(*m*-CBA)Fe^{IV}O–Fe=O}) compared to the HO⁻ ligand (see Fig. 11). We have calculated the $\Delta E(E_{(\pi^*xz)} - E_{(\sigma^*x^2-y^2)})$ energy gap for all seven complexes as 0.931, 0.805, 1.105, 0.511, 0.588, 0.865, and 1.061 eV, respectively, which suggest that the reactivity order of the methane hydroxylation is: **4** > **4a** > **2** > **4b** > **4c** > **1** ≈ **3** (see Fig. S17 in the ESI†). Additionally, DFT calculations show that a two-state reactivity model applies to this series of complexes, in which a triplet

---

Barrier Height for C-H activation (in kJ/mol)
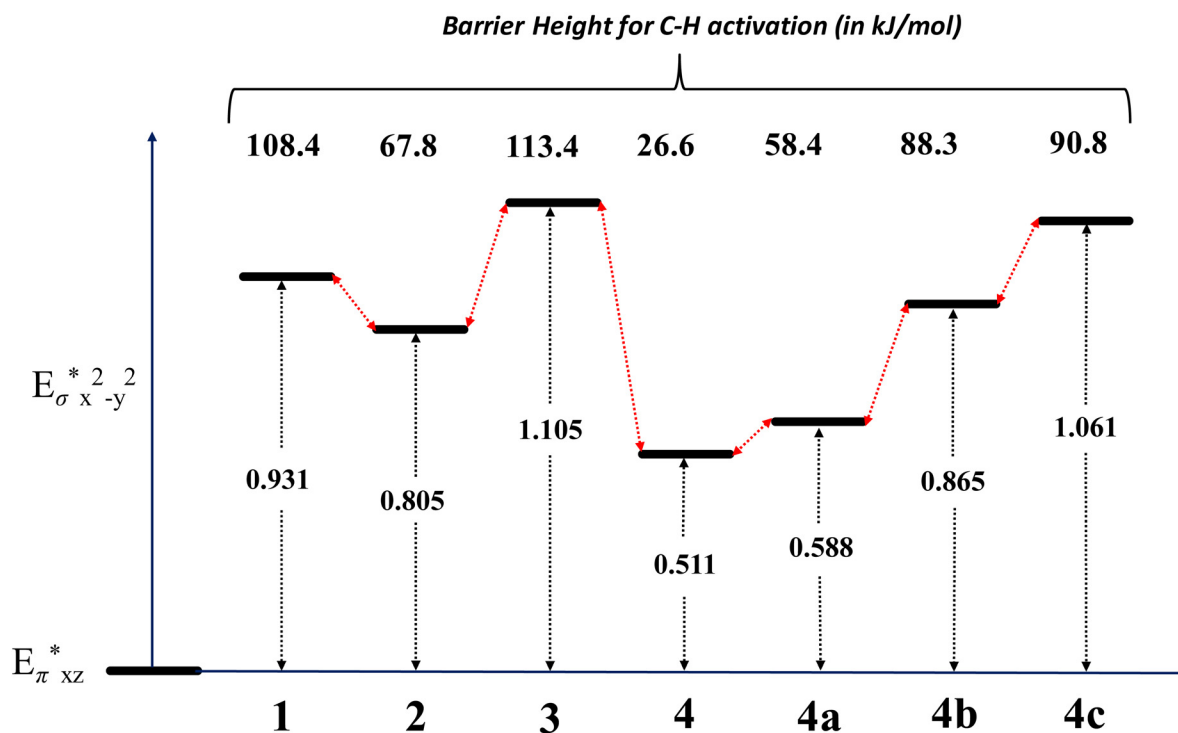
Fig. 11 We computed relative energies of the $E_{\sigma^*x^2-y^2}$ orbital of all seven species. Here, we have plotted the energy difference between $\Delta E(E_{(\pi^*xz)} - E_{(\sigma^*x^2-y^2)})$ *versus* E_{π^*xz}, and E_{π^*xz} is used as a reference for all species. Here, we have used only high-spin structures for calculating energy differences.

ground state and a nearby quintet excited state both contribute to the reactivity of the complexes. Furthermore, the rate of C–H activation increases with a continuous decrease in $\Delta E_{\text{T–Q}}$ (see Table 1).[147,148]

Furthermore, we have carefully looked at the spin density on the O/N atom of the axial ligand from the reactant (**R**) to the transition state (**ts1**), which suggests that the axial ligand also helps to stabilise the newly forming $Fe^{III/IV}$–H bond.[43,149,150] Earlier experimental and theoretical studies of the axial ligand effect on the $[Fe^{IV}(O)(porp^{\bullet+})(X)]$ species demonstrate that the electron-donating group significantly increases the reactivity.[147] For the **1/3** species, we have not observed a spin density change on the axial atom (O2) in the transition state from the reactant, suggesting no flow of electrons during HA-T (see Fig. 4 and 8). Particularly for complex **3** possessing dimeric Fe^{IV} units, no alteration in the spin density was noted, and this suggests that there is no electronic cooperativity between two iron centres that was witnessed for several dinuclear Fe^{IV}=O species earlier. On the other hand, for species **2**, the spin density values on the O(1) atom change from the reactant (−0.46) to the transition state (0.22), suggesting the flow of electrons from the axial atom (see Fig. 6b) during the HA-T. It is clear that the axial ligand stabilizes the newly formed Fe^{IV}–OH bond, indicating that the intermediate formed is endothermic (45.0 kJ mol^{-1}) in nature, unlike species **1** and **3** (see Fig. 10). In comparison, for species **4**, the spin density values on the N(1)/Fe^{IV}/O(1) atoms transfer from the reactant (0.11/−0.89/−0.05) to the transition state (−0.18/−0.78/−0.02), suggesting a significant flow of electron from the substrate to the reactive centre during the HA-T. Here, the $\{Fe^{IV}(O)(por^{\bullet+})\}$ unit has the $\{(Por)(m\text{-CBA})Fe^{IV}(N)\}$ unit as the axial ligand and the μ-nitrido groups possessing significant spin density and its accumulation of electrons from the $\{(Por)(m\text{-CBA})Fe^{IV}\}$ unit clearly reveals the cooperation between two iron centres in the reactivity.[44,45] The spin density plot (see Fig. 1h) clearly reveals a spin polarisation at the Fe^{IV}=O center (gain of spin density on the Fe^{IV}=O unit at the transition state) and the existence of cooperative oxidising ability of the combined unit. Additionally, the second unit stabilizes the newly formed Fe^{III}O–H bond, thereby significantly increasing the reactivity since an electron-donating group is in the axial position, supporting our findings. One reason for the enhanced reactivity observed with species **4** is that the intermediate species is slightly endothermic in nature compared to species **1**, **2**, and **3**.

Furthermore, an even more dramatic rate enhancement was observed when the anionic donor was changed from μ-oxo in species **3** to more electron-donating μ-nitrido, which converts CH_4 to HCOOH with a TON of ~14. This confirms the remarkable oxidising properties of complex **4**. This suggests that the μ-nitrido has more electron-donating power as an axial ligand compared to the μ-oxo.[59,60] Thus, our calculated results suggested that the poorest electron donor among the axial ligands is $(Por)(m\text{-CBA})Fe^{IV}O^-$ and the strongest is $\{(Por)(m\text{-CBA})Fe^{IV}N\}^-$ followed by the HO^- group. This is also supported by the axial ligand effect reported experimentally by

Sastri *et al.*[151] Species **3** (*i*1046) has a longer C–H bond and shorter O–H bond distances, and this suggests a product-like TS in contrast to species **4** (*i*1292). The calculated PES around the TS will be sharper, narrower, and more sensitive for **4** than for **3**, which is in satisfying agreement with the trend in reactivity that was observed experimentally (see Fig. 10). Furthermore, we have also compared the reactivity order of methane oxidation using four different model species (**4** to **4c**). We find that the computed barrier height for C–H activation decreases from **4a** to **4c**, suggesting that the nitrido (≡N) group has a greater electron-donating power as an axial ligand than the −NH/NH$_2$ groups. Similarly, we also made a comparison between **4** and **4a** for methane activation, which shows that the barrier height of **4** (reactant-like transition state) is lower than that of **4a** (product-like transition state). This clearly suggests that $\{(Por)(m\text{-CBA})Fe^{IV}N\}^-$ is the best axial ligand as compared to the nitrido (≡N) group. The presence of electronic cooperativity in species **4** significantly reduces the barrier height of the reaction.

Correlation with experiments

Our results are fully supported by the experiments where four different Fe^{IV}=O species have been proposed as the oxidants for the hydroxylation of methane. Recently, van Eldik and co-workers established that species Cpd I is more reactive toward the HAT from the substrate than Cpd II.[23] Our calculations also support this because species **2** (the model system of Cpd I) has a lower barrier height (C–H activation as well as O–C rebound step) for methane hydroxylation than species **1** (the model system of Cpd II). It has been found that the formed intermediate species **1** (**int1**) is highly unstable when compared to species **2**, suggesting that it is too slow in the oxidant to activate methane. Furthermore, the kinetic experiments performed on μ-oxo diiron–oxo (**3**), μ-carbido diiron–oxo, and μ-nitrido diiron–oxo (**4**) reveal a very higher barrier height for the C–H activation and O–C bond formation of μ-oxo diiron–oxo species.[7] For the μ-nitrido diiron–oxo species, the calculated barrier heights for the C–H activation step are found to be 26.6 kJ mol^{-1}, while the rebound step is found to be the barrier-less process. These calculations suggest that the μ-oxo diiron–oxo species have very sluggish oxidising capabilities. Our calculated data reveal that a very high energy barrier height of the O–C rebound step makes methane formation very difficult, especially for species **1** and **3**, and therefore they are likely to perform the desaturation reaction. Furthermore, we have found that both the barrier heights and formed intermediate energies of species **2** are slightly higher than those of species **4**, and thus the μ-nitrido dinuclear-oxo species (**4**) is the best catalyst among the four complexes described above.[19]

Conclusions

In this work, using DFT and *ab initio* DLPNO–CCSD(T) calculations, we have studied a variety of high-valent iron–oxo species (**1–4**) and the corresponding models to understand

how various structural and electronic effects modulate the reactivity of these species.

(i) The ground state of $[(HO)Fe^{IV}(O)(Por)]^-$ (**1**) is the triplet state, followed by the quintet state with a 38.6 kJ mol⁻¹ energy gap. The small energy gap warrants a two-state reactivity scenario, but our computed barrier heights for C–H activation (108.4 kJ mol⁻¹ at the triplet surface) and –OH rebound steps (132.7 kJ mol⁻¹) make this reaction prohibitively difficult. Clearly, heme $Fe^{IV}{=}O$ groups with axial –OH groups do not possess sufficient oxidising power, as one-electron reduction leads to a Fe(III)–OH species that tends to reduce the nucleophilicity and inhibit the –OH rebound. A desaturation of alkanes possessing weaker C–H bonds is possible with such species.

(ii) In $[(HO)Fe^{IV}(O)(Por^{\bullet+})]$ (**2**), the quartet ($S = 3/2$) state is found to be the ground state, while the other spin states (below ~28 kJ mol⁻¹) are not far from the ground state. Here, two-state reactivity is observed, and a small activation energy for the C–H bond activation of methane (67.8 kJ mol⁻¹) is observed at the doublet surface. This is due to the presence of $^{\bullet+}$ at the porphyrin ring, which facilitates the flow of electrons from the –OH group towards the Fe(IV) centre during HAT. The nature of all spin states reveals a π-type reactivity operating for species **2**, and the orbital control of the reaction is responsible for the significant reduction of barrier height in an intermediate-spin state of $Fe^{IV}{=}O$ compared to a high-spin state. The formation of the radical intermediate is found to be endothermic in nature in all spin states, while the rebound step has a lower barrier height (47.3 kJ mol⁻¹) than the C–H bond activation at the doublet surface. Overall this species is capable of oxidising methane, and experiments also support this fact.

(iii) The dinuclear species $[(Por)(m\text{-CBA})Fe^{IV}(\mu\text{-O})Fe^{IV}(O)(Por^{\bullet+})]$ (**3**) is found to possess a doublet as the ground state arising from antiferromagnetically coupled intermediate spin states. Elaborate bonding analysis reveals that the Fe(IV)=O centre does not accept electrons from the μ-oxo oxygen atom, even though it accepts the donation from the Fe(IV)–m-CBA unit. Thus, the important electronic cooperativity between two Fe centres *via* the μ-oxo group is missing, *i.e.* both barriers (113.4 kJ mol⁻¹ for C–H activation and 126.3 kJ mol⁻¹ for the rebound step) are very high in energy. The strong axial σ-donor ligands increase the barrier height in the high-spin state, *i.e.* the intermediate-spin ground state did not cross the high-spin state across the entire potential energy surface, suggesting that the single-state reactivity is observed for species **3**. The formation of intermediate species for **3** is expected to be highly endothermic in nature in all spin states, with the lowest energy at the doublet surface of 90.0 kJ mol⁻¹. This species is found to be unreactive towards methane to yield little hydroxylated product, and this is due to the higher barriers for C–H activation as well as the rebound step. This also supports the experimental data.

(iv) The model system of species **4a–4c** originates from species **4**, while the axial group $[(Por)(m\text{-CBA})Fe^{IV}(\mu\text{-N})]$ is simply modelled as N (**4a**), NH (**4b**), and NH_2 (**4c**). The calculated ground state for **4a**/**4b**/**4c** was found to be the high-spin

^{6}**4a**$_{(hs)}$/intermediate spin ^{4}**4b**$_{(is)}$/intermediate spin ^{2}**4c**$_{(is)}$ state and is also supported by DLPNO–CCSD(T) calculations. The calculated barrier heights toward the C–H bond activation of methane for the **4a–4c** species are found to be 58.4, 88.3 and 90.6 kJ mol⁻¹ at the ^{4}**ts1**$_{(is)}$ surface, respectively. Species **4a** has the lowest barrier height compared to **4b**/**4c** due to the stronger trans effect, increasing the Fe–O bond length, leading to a better catalyst for C–H activation. Species **4** has the lowest activation energy among all, and this is due to the presence of a stronger axial effect of the $[\{(Por)(m\text{-CBA})Fe^{IV}N\}^-]$ moiety. This is due to the presence of electronic cooperativity in species **4**, which plays an important role in reducing the barrier height of the C–H bond during the methane hydroxylation reaction, as suggested earlier. From mononuclear to dinuclear iron–oxo species, the enhanced nuclearity and electronic cooperativity also help in increasing the reactivity towards methane activation. Finally, the reactivity order found in the methane hydroxylation is **4** >**4a** >**2** >**4b** >**4c** >**1** ≈**3**.

Conflicts of interest

There are no conflicts to declare.

Acknowledgements

References

1 A. E. Shilov and G. B. Shul'pin, *Chem. Rev.*, 1997, **97**, 2879–2932.

2 R. A. Periana, D. J. Taube, S. Gamble, H. Taube, T. Satoh and H. Fujii, *Science*, 1998, **280**, 560–564.

3 A. Gunay and K. H. Theopold, *Chem. Rev.*, 2010, **110**, 1060–1081.

4 M. Costas, *Coord. Chem. Rev.*, 2011, **255**, 2912–2932.

5 W. Nam, *Acc. Chem. Res.*, 2007, **40**, 522–531.

6 S. P. de Visser, *J. Am. Chem. Soc.*, 2006, **128**, 9813–9824.

7 A. B. Sorokin, E. V. Kudrik and D. Bouchu, *Chem. Commun.*, 2008, 2562–2564.

8 M. Puri and L. Que Jr., *Acc. Chem. Res.*, 2015, **48**, 2443–2452.

9 L. Que and Y. Dong, *Acc. Chem. Res.*, 1996, **29**, 190–196.

10 W. N. Oloo and L. Que Jr., *Acc. Chem. Res.*, 2015, **48**, 2612–2621.

11 S. Fukuzumi, T. Kojima, Y.-M. Lee and W. Nam, *Coord. Chem. Rev.*, 2017, **333**, 44–56.

12 J. P. Biswas, S. Guin and D. Maiti, *Coord. Chem. Rev.*, 2020, **408**, 213174.

13 J. Hohenberger, K. Ray and K. Meyer, *Nat. Commun.*, 2012, **3**, 1–13.

14 A. Borovik, *Chem. Soc. Rev.*, 2011, **40**, 1870–1874.

15 X. Shan and L. Que Jr., *J. Inorg. Biochem.*, 2006, **100**, 421–433.

16 R. Kumar, B. Pandey, A. Sen, M. Ansari, S. Sharma and G. Rajaraman, *Coord. Chem. Rev.*, 2020, **419**, 213397.

17 J. Rittle and M. T. Green, *Science*, 2010, **330**, 933–937.

18 I. G. Denisov, T. M. Makris, S. G. Sligar and I. Schlichting, *Chem. Rev.*, 2005, **105**, 2253–2278.

19 J. T. Groves, R. C. Haushalter, M. Nakamura, T. E. Nemo and B. Evans, *J. Am. Chem. Soc.*, 1981, **103**, 2884–2886.

20 J. T. Groves, *Proc. Natl. Acad. Sci. U. S. A.*, 2003, **100**, 3569–3574.

21 Y. Urano, T. Higuchi, M. Hirobe and T. Nagano, *J. Am. Chem. Soc.*, 1997, **119**, 12008–12009.

22 W. Nam, S.-E. Park, I. K. Lim, M. H. Lim, J. Hong and J. Kim, *J. Am. Chem. Soc.*, 2003, **125**, 14674–14675.

23 C. Fertinger, N. Hessenauer-Ilicheva, A. Franke and R. van Eldik, *Chem. – Eur. J.*, 2009, **15**, 13435–13440.

24 X. X. Li, V. Postils, W. Sun, A. S. Faponle, M. Solà, Y. Wang, W. Nam and S. P. De Visser, *Chem. – Eur. J.*, 2017, **23**, 6406–6418.

25 J. T. Groves, Z. Gross and M. K. Stern, *Inorg. Chem.*, 1994, **33**, 5065–5072.

26 M. T. Green, J. H. Dawson and H. B. Gray, *Science*, 2004, **304**, 1653–1656.

27 M. J. Field, P. H. Oyala and M. T. Green, *J. Am. Chem. Soc.*, 2022, **144**, 19272–19283.

28 M. A. Ehudin, L. B. Gee, S. Sabuncu, A. Braun, P. Moënne-Loccoz, B. Hedman, K. O. Hodgson, E. I. Solomon and K. D. Karlin, *J. Am. Chem. Soc.*, 2019, **141**, 5942–5960.

29 M. A. Ehudin, D. A. Quist and K. D. Karlin, *J. Am. Chem. Soc.*, 2019, **141**, 12558–12569.

30 P. Comba, M. Maurer and P. Vadivelu, *Inorg. Chem.*, 2009, **48**, 10389–10396.

31 P. Comba, Y.-M. Lee, W. Nam and A. Waleska, *Chem. Commun.*, 2014, **50**, 412–414.

32 M. Jaccob, P. Comba, M. Maurer, P. Vadivelu and P. Venuvanalingam, *Dalton Trans.*, 2011, **40**, 11276–11281.

33 S. Fukuzumi, Y. Morimoto, H. Kotani, P. Naumov, Y.-M. Lee and W. Nam, *Nat. Chem.*, 2010, **2**, 756–759.

34 A. J. McGown, W. D. Kerber, H. Fujii and D. P. Goldberg, *J. Am. Chem. Soc.*, 2009, **131**, 8040–8048.

35 A. R. McDonald and L. Que Jr., *Coord. Chem. Rev.*, 2013, **257**, 414–428.

36 D. Kass, T. Corona, K. Warm, B. Braun-Cula, U. Kuhlmann, E. Bill, S. Mebs, M. Swart, H. Dau and M. Haumann, *J. Am. Chem. Soc.*, 2020, **142**, 5924–5928.

37 A. Lindhorst, S. Haslinger and F. E. Kühn, *Chem. Commun.*, 2015, **51**, 17193–17212.

38 J. P. Biswas, M. Ansari, A. Paik, S. Sasmal, S. Paul, S. Rana, G. Rajaraman and D. Maiti, *Angew. Chem., Int. Ed.*, 2021, **60**, 14030–14039.

39 M. Okamura, M. Kondo, R. Kuga, Y. Kurashige, T. Yanai, S. Hayami, V. K. Praneeth, M. Yoshida, K. Yoneda and S. Kawata, *Nature*, 2016, **530**, 465–468.

40 V. K. Praneeth, M. Kondo, M. Okamura, T. Akai, H. Izu and S. Masaoka, *Chem. Sci.*, 2019, **10**, 4628–4639.

41 W. C. Ellis, N. D. McDaniel, S. Bernhard and T. J. Collins, *J. Am. Chem. Soc.*, 2010, **132**, 10990–10991.

42 G. De Ruiter, N. B. Thompson, M. K. Takase and T. Agapie, *J. Am. Chem. Soc.*, 2016, **138**, 1486–1489.

43 M. G. Quesne, D. Senthilnathan, D. Singh, D. Kumar, P. Maldivi, A. B. Sorokin and S. P. De Visser, *ACS Catal.*, 2016, **6**, 2230–2243.

44 M. Ansari, D. Senthilnathan and G. Rajaraman, *Chem. Sci.*, 2020, **11**, 10669–10687.

45 M. Ansari, N. Vyas, A. Ansari and G. Rajaraman, *Dalton Trans.*, 2015, **44**, 15232–15243.

46 M. G. Quesne, F. Silveri, N. H. De Leeuw and C. R. A. Catlow, *Front. Chem.*, 2019, **7**, 182.

47 A. B. Sorokin, *Catal. Today*, 2021, **373**, 38–58.

48 D. M. Kurtz Jr., *Chem. Rev.*, 1990, **90**, 585–606.

49 T. G. Spiro and R. S. Czernuszewicz, in *Methods in enzymology*, Elsevier, 1995, vol. 246, pp. 416–460.

50 A. C. Rosenzweig, P. Nordlund, P. M. Takahara, C. A. Frederick and S. J. Lippard, *Chem. Biol.*, 1995, **2**, 409–418.

51 B. Mauerer, J. Crane, J. Schuler, K. Wieghardt and B. Nuber, *Angew. Chem., Int. Ed. Engl.*, 1993, **32**, 289–291.

52 I. Fujita, L. K. Hanson, F. A. Walker and J. Fajer, *J. Am. Chem. Soc.*, 1983, **105**, 3296–3300.

53 R. Kumar, A. Ansari and G. Rajaraman, *Chem. – Eur. J.*, 2018, **24**, 6818–6827.

54 P. Afanasiev, E. V. Kudrik, J.-M. M. Millet, D. Bouchu and A. B. Sorokin, *Dalton Trans.*, 2011, **40**, 701–710.

55 L. P. Cailler, M. Clémancey, J. Barilone, P. Maldivi, J.-M. Latour and A. B. Sorokin, *Inorg. Chem.*, 2019, **59**, 1104–1116.

56 E. V. Kudrik, P. Afanasiev, L. X. Alvarez, P. Dubourdeaux, M. Clémancey, J.-M. Latour, G. Blondin, D. Bouchu, F. Albrieux, S. E. Nefedov and A. B. Sorokin, *Nat. Chem.*, 2012, **4**, 1024–1029.

57 H. Basch, K. Mogi, D. G. Musaev and K. Morokuma, *J. Am. Chem. Soc.*, 1999, **121**, 7249–7256.

58 P. E. Siegbahn and R. H. Crabtree, *J. Am. Chem. Soc.*, 1997, **119**, 3103–3113.

59 C. Colomban, E. V. Kudrik, V. Briois, J. C. Shwarbrick, A. B. Sorokin and P. Afanasiev, *Inorg. Chem.*, 2014, **53**, 11517–11530.

60 R. Silaghi-Dumitrescu, S. V. Makarov, M.-M. Uta, I. A. Dereven'kov and P. A. Stuzhin, *New J. Chem.*, 2011, **35**, 1140–1145.

61 A. Ansari, M. Ansari, A. Singha and G. Rajaraman, *Chem. – Eur. J.*, 2017, **23**, 10110–10125.

62 C. E. Schulz, R. G. Castillo, D. A. Pantazis, S. DeBeer and F. Neese, *J. Am. Chem. Soc.*, 2021, **143**, 6560–6577.

63 M. J. e. a. Frisch, *Gaussian 09, revision 02*, Gaussian, Inc., Wallingford, CT, 2009.

64 S. Grimme, *J. Comput. Chem.*, 2006, **27**, 1787–1799.

65 A. Pabis, I. Geronimo and P. Paneth, *J. Phys. Chem. B*, 2014, **118**, 3245–3256.

66 A. Ansari, A. Kaushik and G. Rajaraman, *J. Am. Chem. Soc.*, 2013, **135**, 4235–4249.

67 A. Ansari and G. Rajaraman, *Phys. Chem. Chem. Phys.*, 2014, **16**, 14601–14613.

68 C. Wang, C. Zhao, L. Hu and H. Chen, *J. Phys. Chem. Lett.*, 2016, **7**, 4427–4432.

69 C. Zhao and H. Chen, *ACS Catal.*, 2017, **7**, 3521–3531.

70 X. Sun, X. Sun, C. Geng, H. Zhao and J. Li, *J. Phys. Chem. A*, 2014, **118**, 7146–7158.

71 H. Chen, W. Lai and S. Shaik, *J. Phys. Chem. Lett.*, 2010, **1**, 1533–1540.

72 A. Ghosh, *J. Biol. Inorg. Chem.*, 2006, **11**, 712–724.

73 P. J. Hay and W. R. Wadt, *J. Chem. Phys.*, 1985, **82**, 299–310.

74 W. J. Hehre, R. Ditchfield and J. A. Pople, *J. Chem. Phys.*, 1972, **56**, 2257–2261.

75 A. Schäfer, H. Horn and R. Ahlrichs, *J. Chem. Phys.*, 1992, **97**, 2571–2577.

76 G. A. Zhurko, *ChemCraft software, version 1.6*, 2014.

77 J. Tomasi, B. Mennucci and R. Cammi, *Chem. Rev.*, 2005, **105**, 2999–3094.

78 L. Noodleman, *J. Chem. Phys.*, 1981, **74**, 5737–5743.

79 L. Noodleman and E. R. Davidson, *Chem. Phys.*, 1986, **109**, 131–143.

80 F. Neese, *Wiley Interdiscip. Rev.: Comput. Mol. Sci.*, 2012, **2**, 73–78.

81 S. E. Neale, D. A. Pantazis and S. A. Macgregor, *Dalton Trans.*, 2020, **49**, 6478–6487.

82 F. Neese, *Wiley Interdiscip. Rev.: Comput. Mol. Sci.*, 2018, **8**, e1327.

83 P. Paiva, M. J. Ramos and P. A. Fernandes, *J. Comput. Chem.*, 2020, **41**, 2459–2468.

84 X. Huang and J. T. Groves, *Chem. Rev.*, 2017, **118**, 2491–2553.

85 Y. Watanabe and J. T. Groves, in *The Enzymes*, Elsevier, 1992, vol. 20, pp. 405–452.

86 D. Mandon, R. Weiss, K. Jayaraj, A. Gold, J. Terner, E. Bill and A. Trautwein, *Inorg. Chem.*, 1992, **31**, 4404–4409.

87 T. Wolter, W. Meyer-Klaucke, M. Müther, D. Mandon, H. Winkler, A. X. Trautwein and R. Weiss, *J. Inorg. Biochem.*, 2000, **78**, 117–122.

88 A. Dey and A. Ghosh, *J. Am. Chem. Soc.*, 2002, **124**, 3206–3207.

89 A. Rosa and G. Ricciardi, *Inorg. Chem.*, 2012, **51**, 9833–9845.

90 G. Ricciardi, E. J. Baerends and A. Rosa, *ACS Catal.*, 2016, **6**, 568–579.

91 B. Meunier, S. P. De Visser and S. Shaik, *Chem. Rev.*, 2004, **104**, 3947–3980.

92 S. Shaik, D. Kumar, S. P. de Visser, A. Altun and W. Thiel, *Chem. Rev.*, 2005, **105**, 2279–2328.

93 A. S. Chowdhury, H. S. Ali, A. S. Faponle and S. P. de Visser, *Phys. Chem. Chem. Phys.*, 2020, **22**, 27178–27190.

94 M. T. Green, *J. Am. Chem. Soc.*, 1998, **120**, 10772–10773.

95 P. Comba, D. Faltermeier, S. Krieg, B. Martin and G. Rajaraman, *Dalton Trans.*, 2020, **49**, 2888–2894.

96 F. Neese, *J. Biol. Inorg. Chem.*, 2006, **11**, 702–711.

97 F. Neese, *Coord. Chem. Rev.*, 2009, **253**, 526–563.

98 A. Ansari, A. Kaushik and G. Rajaraman, *J. Am. Chem. Soc.*, 2013, **135**, 4235–4249.

99 H. Chen, W. Lai and S. Shaik, *J. Phys. Chem. Lett.*, 2010, **1**, 1533–1540.

100 F. Saiz and L. Bernasconi, *Phys. Chem. Chem. Phys.*, 2020, **22**, 12821–12830.

101 H. Hirao, N. Thellamurege and X. Zhang, *Front. Chem.*, 2014, **2**, 14.

102 A. Ghosh, J. Almlof and L. Que Jr., *J. Phys. Chem.*, 1994, **98**, 5576–5579.

103 F. Neese, D. G. Liakos and S. Ye, *J. Biol. Inorg. Chem.*, 2011, **16**, 821–829.

104 B. M. Flöser, Y. Guo, C. Riplinger, F. Tuczek and F. Neese, *J. Chem. Theory Comput.*, 2020, **16**, 2224–2235.

105 M. Drosou, C. A. Mitsopoulou and D. A. Pantazis, *J. Chem. Theory Comput.*, 2022, **18**, 3538–3548.

106 Q. M. Phung, C. Martín-Fernández, J. N. Harvey and M. Feldt, *J. Chem. Theory Comput.*, 2019, **15**, 4297–4304.

107 Q. M. Phung, M. Feldt, J. N. Harvey and K. Pierloot, *J. Chem. Theory Comput.*, 2018, **14**, 2446–2455.

108 B. Mondal, F. Neese, E. Bill and S. Ye, *J. Am. Chem. Soc.*, 2018, **140**, 9531–9544.

109 A. Ghosh, E. Tangen, H. Ryeng and P. R. Taylor, *Eur. J. Inorg. Chem.*, 2004, **2004**, 4555–4560.

110 D. Kumar, G. N. Sastry and S. P. De Visser, *J. Phys. Chem. B*, 2012, **116**, 718–730.

111 C. W. Lee, M. Q. E. Mubarak, A. P. Green and S. P. De Visser, *Int. J. Mol. Sci.*, 2020, **21**, 7133.

112 M. Lučić, D. A. Svistunenko, M. T. Wilson, A. K. Chaplin, B. Davy, A. Ebrahim, D. Axford, T. Tosha, H. Sugimoto, S. Owada, F. S. N. Dworkowski, I. Tews, R. L. Owen, M. A. Hough and J. A. R. Worrall, *Angew. Chem., Int. Ed.*, 2020, **59**, 21656–21662.

113 A. P. Ledray, C. M. Krest, T. H. Yosca, K. Mittra and M. T. Green, *J. Am. Chem. Soc.*, 2020, **142**, 20419–20425.

114 M. Puri and L. Que, *Acc. Chem. Res.*, 2015, **48**, 2443–2452.

115 S. A. Wilson, J. Chen, S. Hong, Y.-M. Lee, M. Clémancey, R. Garcia-Serres, T. Nomura, T. Ogura, J.-M. Latour, B. Hedman, K. O. Hodgson, W. Nam and E. I. Solomon, *J. Am. Chem. Soc.*, 2012, **134**, 11791–11806.

116 S. Shaik, H. Chen and D. Janardanan, *Nat. Chem.*, 2012, **4**, 511–511.

117 S. F. Ye and F. Neese, *Proc. Natl. Acad. Sci. U. S. A.*, 2011, **108**, 1228–1233.

118 R. M. Badger, *J. Chem. Phys.*, 1935, **3**, 710–714.

119 M. T. Green, *J. Am. Chem. Soc.*, 2006, **128**, 1902–1906.

120 K.-B. Cho, X. Wu, Y.-M. Lee, Y. H. Kwon, S. Shaik and W. Nam, *J. Am. Chem. Soc.*, 2012, **134**, 20222–20225.

121 E. Derat and S. Shaik, *J. Am. Chem. Soc.*, 2006, **128**, 8185–8198.

122 K. L. Stone, L. M. Hoffart, R. K. Behan, C. Krebs and M. T. Green, *J. Am. Chem. Soc.*, 2006, **128**, 6147–6153.

123 S. Ye and F. Neese, *Proc. Natl. Acad. Sci. U. S. A.*, 2011, **108**, 1228–1233.

124 S. Shaik, H. Hirao and D. Kumar, *Acc. Chem. Res.*, 2007, **40**, 532–542.

125 S. Shaik and S. P. De Visser, in *Cytochrome P450: Structure, Mechanism, and Biochemistry*, ed. P. R. Ortiz de Montellano, Springer US, Boston, MA, 2005, pp. 45–85, DOI: 10.1007/0-387-27447-2_2.

126 S. Shaik, S. Cohen, S. P. De Visser, P. K. Sharma, D. Kumar, S. Kozuch, F. Ogliaro and D. Danovich, *Eur. J. Inorg. Chem.*, 2004, **2004**, 207–226.

127 D. Kumar, S. P. de Visser, P. K. Sharma, S. Cohen and S. Shaik, *J. Am. Chem. Soc.*, 2004, **126**, 1907–1920.

128 K. Mittra and M. T. Green, *J. Am. Chem. Soc.*, 2019, **141**, 5504–5510.

129 T. H. Yosca, J. Rittle, C. M. Krest, E. L. Onderko, A. Silakov, J. C. Calixto, R. K. Behan and M. T. Green, *Science*, 2013, **342**, 825–829.

130 M. Jaccob, A. Ansari, B. Pandey and G. Rajaraman, *Dalton Trans.*, 2013, **42**, 16518–16526.

131 P. Barman, A. K. Vardhaman, B. Martin, S. J. Wörner, C. V. Sastri and P. Comba, *Angew. Chem., Int. Ed.*, 2015, **54**, 2095–2099.

132 S. Shaik, S. P. de Visser, F. Ogliaro, H. Schwarz and D. Schröder, *Curr. Opin. Chem. Biol.*, 2002, **6**, 556–567.

133 S. P. de Visser, F. Ogliaro, P. K. Sharma and S. Shaik, *J. Am. Chem. Soc.*, 2002, **124**, 11809–11826.

134 D. Usharani, D. C. Lacy, A. S. Borovik and S. Shaik, *J. Am. Chem. Soc.*, 2013, **135**, 17090–17104.

135 D. Janardanan, Y. Wang, P. Schyman, L. Que Jr. and S. Shaik, *Angew. Chem., Int. Ed.*, 2010, **49**, 3342–3345.

136 E. R. Johnson, S. Keinan, P. Mori-Sánchez, J. Contreras-García, A. J. Cohen and W. Yang, *J. Am. Chem. Soc.*, 2010, **132**, 6498–6506.

137 S. Tsuzuki, K. Honda, T. Uchimaru and M. Mikami, *J. Chem. Phys.*, 2005, **122**, 144323.

138 O. Takahashi, Y. Kohno and M. Nishio, *Chem. Rev.*, 2010, **110**, 6049–6076.

139 D. P. Malenov, G. V. Janjić, D. Ž. Veljković and S. D. Zarić, *Comput. Theor. Chem.*, 2013, **1018**, 59–65.

140 Q. Wang, X. Chen, G. Li, Q. Chen, Y.-F. Yang and Y.-B. She, *J. Org. Chem.*, 2019, **84**, 13755–13763.

141 K. L. Bay, Y.-F. Yang and K. N. Houk, *J. Org. Chem.*, 2018, **83**, 14786–14790.

142 J. Contreras-García, E. R. Johnson, S. Keinan, R. Chaudret, J.-P. Piquemal, D. N. Beratan and W. Yang, *J. Chem. Theory Comput.*, 2011, **7**, 625–632.

143 R. S. Proctor, A. C. Colgan and R. J. Phipps, *Nat. Chem.*, 2020, **12**, 990–1004.

144 M. A. Hussain, D. Vijay and G. N. Sastry, *J. Comput. Chem.*, 2016, **37**, 366–377.

145 V. B. Medaković, G. A. Bogdanović, M. K. Milčić, G. V. Janjić and S. D. Zarić, *J. Inorg. Biochem.*, 2012, **117**, 157–163.

146 Y. Kang, H. Chen, Y. J. Jeong, W. Lai, E. H. Bae, S. Shaik and W. Nam, *Chem. – Eur. J.*, 2009, **15**, 10039–10046.

147 C. V. Sastri, J. Lee, K. Oh, Y. J. Lee, J. Lee, T. A. Jackson, K. Ray, H. Hirao, W. Shin, J. A. Halfen, K. Kim, L. Que Jr., S. Shaik and W. Nam, *Proc. Natl. Acad. Sci. U. S. A.*, 2007, **104**, 19181–19186.

148 F. De Angelis, N. Jin, R. Car and J. T. Groves, *Inorg. Chem.*, 2006, **45**, 4268–4276.

149 S. P. de Visser, D. Kumar, S. Cohen, R. Shacham and S. Shaik, *J. Am. Chem. Soc.*, 2004, **126**, 8362–8363.

150 S. P. De Visser, *J. Am. Chem. Soc.*, 2010, **132**, 1087–1097.

151 T. A. Jackson, J.-U. Rohde, M. S. Seo, C. V. Sastri, R. DeHont, A. Stubna, T. Ohta, T. Kitagawa, E. Münck and W. Nam, *J. Am. Chem. Soc.*, 2008, **130**, 12394–12407.